



ELSEVIER

Contents lists available at ScienceDirect

Journal of Petroleum Science and Engineering

journal homepage: www.elsevier.com/locate/petrol

Maximization of wave motion within a hydrocarbon reservoir for wave-based enhanced oil recovery

C. Jeong^{a,*}, L.F. Kallivokas^b, S. Kucukcoban^c, W. Deng^d, A. Fathi^b^a Department of Civil Engineering, The Catholic University of America, Washington, DC 20064, USA^b Department of Civil, Architectural and Environmental Engineering, The University of Texas at Austin, Austin, TX 78712, USA^c Stress Engineering Services, Houston, TX 77041, USA^d Department of Civil, Architectural and Environmental Engineering, Missouri University of Science and Technology, Rolla, MO 65409, USA

ARTICLE INFO

Article history:

Received 2 December 2014

Accepted 15 March 2015

Available online 21 March 2015

Keywords:

Wave-based enhanced oil recovery

Wave energy focusing

Finite elements

PDE-constrained-optimization

Perfectly-Matched-Layer (PML)

ABSTRACT

We discuss a systematic methodology for investigating the feasibility of mobilizing oil droplets trapped within the pore space of a target reservoir region by optimally directing wave energy to the region of interest. The motivation stems from field and laboratory observations, which have provided sufficient evidence suggesting that wave-based reservoir stimulation could lead to economically viable oil recovery.

Using controlled active surface wave sources, we first describe the mathematical framework necessary for identifying optimal wave source signals that can maximize a desired motion metric (kinetic energy, particle acceleration, etc.) at the target region of interest. We use the apparatus of partial-differential-equation (PDE)-constrained optimization to formulate the associated inverse-source problem, and deploy state-of-the-art numerical wave simulation tools to resolve numerically the associated discrete inverse problem.

Numerical experiments with a synthetic subsurface model featuring a shallow reservoir show that the optimizer converges to wave source signals capable of maximizing the motion within the reservoir. The spectra of the wave sources are dominated by the amplification frequencies of the formation. We also show that wave energy could be focused within the target reservoir area, while simultaneously minimizing the disturbance to neighboring formations – a concept that can also be exploited in fracking operations.

Lastly, we compare the results of our numerical experiments conducted at the reservoir scale, with results obtained from semi-analytical studies at the granular level, to conclude that, in the case of shallow targets, the optimized wave sources are likely to mobilize trapped oil droplets, and thus enhance oil recovery.

© 2015 Elsevier B.V. All rights reserved.

1. Introduction

Most Enhanced Oil Recovery (EOR) methods rely on gas- or chemical-flooding, which, due to the formation's inherent heterogeneity, can hardly sweep an oil field in its entirety. By contrast, wave-based EOR methods are promising, not only due to their relative cost-effectiveness, but also because the waves used to illuminate a target reservoir can do so rather indiscriminantly, thus impacting regions of otherwise bypassed oil. The key idea behind wave-based EOR is that elastic waves, in whichever way they may have been generated, could potentially “shake” a reservoir strongly enough to mobilize the remaining oil. The mobilized oil can then be recovered by conventional means. The wave sources, typically used in wave-based EOR, include

Vibroiseis equipment atop the ground surface, wellbore hydraulic pumps (Bremmer et al., 2006), and/or wellbore vibrators (Paulsson, 1989; Westermark et al., 2001a).

The potential of wave-based EOR is supported by a set of field observations, which show that elastic waves induce increased production of the remaining oil. For instance, it has been observed that the rate of oil production and/or the oil-water-cut ratio increases during and after seismic events in oil reservoirs situated within the broader region impacted by the earthquake (Steinbrugge and Moran, 1954; Smimova, 1968; Voytov et al., 1972; Osika, 1981). Increased oil production has also been reported during field experiments conducted with wave sources located on the ground surface, or within a wellbore, either in active or in seemingly-depleted oil fields (Kuznetsov et al., 1990, 2002; Kouznetsov et al., 1998; Westermark et al., 2001b; Spanos et al., 2003; Guo et al., 2004; Kostrov and Wooden, 2005, 2008; Zhu and Xutao, 2005; Barabanov and Pavlov, 2009).

* Corresponding author.

E-mail address: jeong@cua.edu (C. Jeong).

Nomenclature

Symbol	Comment		
\mathbf{x}	location	v_s	shear wave velocity
t	time	$\mathbf{f}(\mathbf{x}, t)$	vector of applied forces of a surface wave source
$\mathbf{S}_a(\mathbf{x}, t)$	history of the Cauchy stress tensor in Ω_0	n_f	number of parameters for temporal discretization of $f_2(\mathbf{x}, t)$
$\mathbf{u}_a(\mathbf{x}, t)$	displacement vector in Ω_0	$f_2(\mathbf{x}, t)$	x_2 -directional force function of $\mathbf{f}(\mathbf{x}, t)$
$\mathbf{S}_b(\mathbf{x}, t)$	history of the Cauchy stress tensor outside Ω_0	f_{2_i}	the i th discretized force parameter for temporal approximation of $f_2(\mathbf{x}, t)$
$\mathbf{u}_b(\mathbf{x}, t)$	displacement vector outside Ω_0	$\varphi_i(t)$	the i th shape function for temporal approximation of $f_2(\mathbf{x}, t)$
Ω_0	target inclusion (hydrocarbon reservoir)	$\mathbf{n}(\mathbf{x})$	unit normal to a surface
Ω_{reg}	regular domain: $\Omega \setminus \Omega_{\text{PML}}$	\mathcal{L}	objective functional to be minimized
Ω_{PML}	domain occupied by PML	$\lambda_{u_a}, \lambda_{u_b}, \lambda_F$	Lagrange multiplier vector function
Ω	entire bounded domain used for computation	$\lambda_{S_a}, \lambda_{S_b}$	Lagrange multiplier tensor function
Γ_{fixed}	outer (Dirichlet) boundary of PML	$\lambda_{S_a}^{\text{sym}}$	symmetric part of λ_{S_a}
Γ_{load}	part of the boundary where loads are applied	$\lambda_{S_b}^{\text{sym}}$	symmetric part of λ_{S_b}
Γ_{free}	free surface boundary	\mathcal{A}	Lagrangian functional
Γ_{int}	interface boundary between Ω_0 and Ω_{reg}	δ	variational symbol
\mathcal{D}	fourth-order compliance tensor	$\mathcal{E}(\mathbf{x})$	coefficient of the body force terms in (16) and (20)
$\tilde{\lambda}_e, \tilde{\lambda}_p$	coordinate stretching tensors associated with the PML	ξ	control variable: $\xi = f_{2_i}$
a, b, c	attenuation coefficients associated with the PML	$\mathbf{f}_{(k)}$	an array of force parameters at the k th optimization iteration; see Algorithm 1
λ, μ	Lamé parameters	$\theta_{(k)}$	step length at the k th optimization iteration
E	elastic modulus	α, β	parameters of the optimization algorithm
ν	Poisson's ratio	f	frequency of the loading time signal of a surface wave source
ρ	mass density		
v_p	compressional wave velocity		

In addition to field evidence, there have also been laboratory investigations of the underlying mechanisms of wave-based EOR. It has been argued that reservoir shaking can lead to cross-flow oscillation at the interface between low- and high-permeability areas in highly heterogeneous reservoirs, or in fractured reservoirs. For example, in a heterogeneous reservoir, the elastic waves induce pore-pressure oscillation between layers of different permeability (Bachrach et al., 2001; Huh, 2006) (Fig. 1(a)). Similarly, in a fractured reservoir (Fig. 1(b)), direct application of hydraulic wave sources to a fracture can induce a periodic pressure gradient between a fracture and the surrounding rock matrix, such that transport of the bypassed oil from the rock matrix into the fracture space can be enhanced (Owens and Archer, 1966; Surguchev et al., 2002; Groenenboom et al., 2003; Stirpe et al., 2004; Jeong et al., 2011).

On the other hand, it has been suggested that the seismic waves increase permeability within hydrocarbon formations. Elkhoury et al. (2006) reported that seismic waves can alter the permeability of aquifers by investigating the earthquake-induced phase changes of the responses of water levels in wells to earth tidal strains (Elkhoury et al., 2006). Elkhoury et al. (2011) also presented that permeability within a fractured rock can be increased via the laboratory tests that use fluid flow oscillation of a very low frequency (0.05 Hz). Unblocking pores, by breaking colloidal deposits or mobilizing droplets trapped in pores, is reported to attribute to the wave-induced change of the permeability in rock formation systems (Manga et al., 2012). Geballe et al. (2011) also suggested a permeability-change model of porous permeable rock media, which explained the increase of the permeability, during seismic activities, followed by its decrease, due to relogging of pores.

It has also been suggested that the movement of the pore walls could also mobilize oil droplets trapped in pore spaces (Beresnev and Johnson, 1994; Averbakh et al., 2000; Hilpert et al., 2000; Beresnev, 2006; Beckham et al., 2010). That is, the vibration of pore walls can dislodge the trapped droplets and coalesce them into larger ones, allowing them to be mobilized and flow, as illustrated in Fig. 2. A set of experimental studies, employing

ultrasound waves, have supported the dislodging mechanism of oil droplets by means of shaking of the rock matrix. In these laboratory experiments, ultrasonic waves with frequencies over 20 kHz were exploited to mobilize oil droplets in ill-saturated sandstone core samples, resulting in increased oil production (Amro et al., 2007; Hamida and Babadagli, 2005a,b,c). However, since waves at such high frequencies attenuate rapidly with distance, techniques relying on ultrasound waves are not viable for mobilizing oil droplets at the reservoir scale (Roberts et al., 2001; Roberts and Abdel-Fattah, 2009). On the other hand, a number of laboratory tests have demonstrated dislodging of oil droplets by using elastic or acoustic wave sources at low frequency ranges: Roberts et al. (2001, 2003), Roberts and Abdel-Fattah (2009), and Beckham et al. (2010) showed that dynamic stress, exerted on a solid rock matrix of a sandstone core at low frequencies (10–100 Hz), can release trapped oil droplets; Vogler and Chrysikopoulos (2004) and Thomas and Chrysikopoulos (2007) also showed that acoustic waves of frequencies up to 300 Hz can remove the non-aqueous phase liquid (NAPL) from porous permeable core samples; Spanos et al. (2003) conducted experiments demonstrating that fluid-pressure pulsing at frequencies ranging from 30 Hz to 60 Hz can increase the oil recovery rate from confined sand packs;

In a capillary-trapping model Iassonov and Beresnev (2003) developed, they showed that the inertia force induced by the elastic wave on a trapped oil droplet, should exceed a threshold level in order for the trapped droplet to overcome the capillary force. From subsequent experiments (Li et al., 2005; Beresnev et al., 2011) and numerical simulations at pore scales (Beresnev, 2006; Beresnev and Deng, 2010; Deng and Cardenas, 2013), they concluded that the acceleration of the rock matrix should be in the order of 0.1–10 m/s², or more, to induce oil mobilization. They further showed that such a threshold acceleration level varies depending on a number of parameters: (a) the average size of the pore space; (b) the background pressure gradient; (c) the wave frequency; (d) the viscosity of the remaining oil; and (e) the capillary pressure. To investigate the feasibility of overcoming the

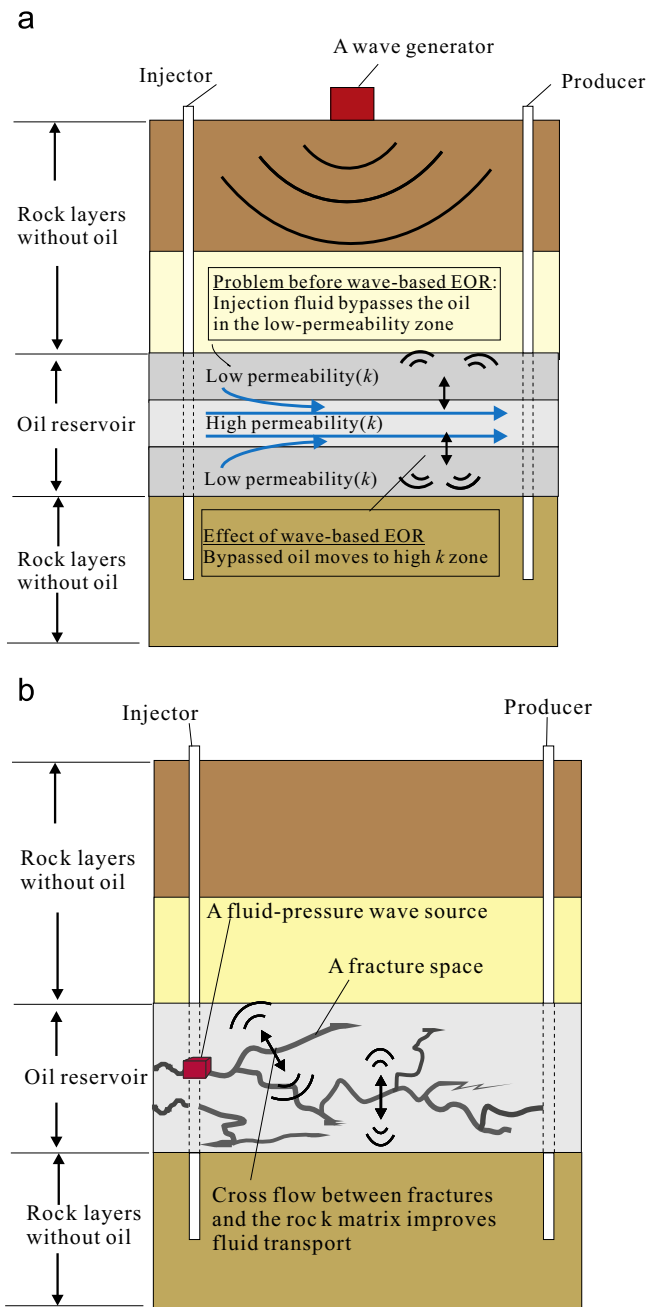


Fig. 1. Wave-induced cross-flow oscillation-based recovery mechanism: (a) elastic wave induces cross-flow oscillation at the interface between different permeability areas and (b) wellbore hydraulic pumps induce cross-flow oscillation at the interface between a fracture space and surrounding rock matrix.

capillary force, one needs to investigate the possibility of generating strong enough wave motions at reservoir scales, such that the acceleration field exceeds the threshold value.

In a preliminary study (Jeong et al., 2010), we proposed an optimization scheme that can *inversely* compute the optimal loading time signal of a ground surface wave source that leads to the maximization of a desired metric, such as the kinetic energy, or, acceleration of a solid rock matrix in a target reservoir formation, when the formation's properties are a priori known. For simplicity, one-dimensional compressional wave physics for a semi-infinite layered medium was considered. This one-dimensional inverse-source identification methodology showed that certain source frequencies lead to the amplification of the wave motion in the target formation. Our numerical optimizer

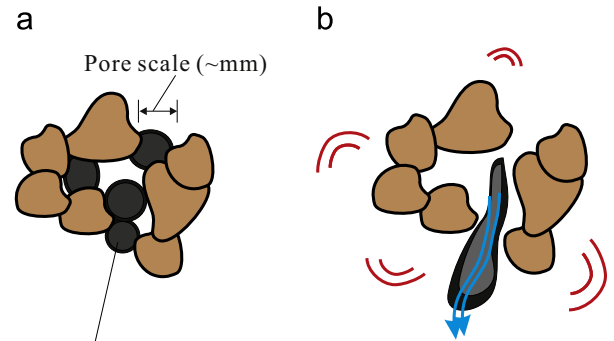


Fig. 2. The mobilization of trapped oil droplets in pore space by the vibration of pore wall surface: (a) oil droplets are captured in the pore space before a wave-based EOR is applied and (b) reservoir shaking mobilizes the oil droplets.

successfully identified near-monochromatic optimal loading time signals with strong dominant frequency components, which coincided with the aforementioned formation amplification frequencies. The inverted-for excitations are well within the capability range of present-day equipment, and induce significant acceleration fields, which, in turn, appear to be large enough to mobilize oil under these one-dimensional assumptions. However, a one-dimensional setting is overly simplistic in at least two ways: first, one-dimensional excitation conditions are impossible to replicate in practice; second, the undamped one-dimensional model we adopted ignores all of the three attenuation mechanisms that are typically associated with the passage of waves in the Earth, i.e., radiation attenuation due to an expanding wave-front, intrinsic attenuation due to wave energy conversion to heat, and apparent attenuation due to scattering effects. As a result, the wave responses predicted by this one-dimensional analysis are overestimated.

Herein, we extend prior work and discuss an inverse-source approach for the more realistic two-dimensional setting. It is assumed that the strip loading is stretched infinitely in a direction that is perpendicular to the cross-sectional plane (see Fig. 4), and the wave motion is undamped. Such two-dimensional loadings can be replicated in practice by using a fleet of Vibroseis equipment, under the assumption of lateral homogeneity, as detailed by Kallivokas et al. (2013). We attempt to address the following questions:

- Are there characteristic amplification frequencies that lead to the maximization of the kinetic energy or acceleration field in a target reservoir?
- Do the optimal loading signals depend on the locations of surface wave sources?
- Can we focus the wave energy into a target formation while minimizing the impact on neighboring formations?
- Do the optimal source signals of multiple wave sources have a different spectrum for each source?
- Is the wave motion, induced by the optimized surface wave sources, large enough to result in the mobilization of trapped oil droplets within a target formation?

To address these questions, we use an inverse source approach to arrive at optimized source signals of wave sources that can maximize certain desired metrics (e.g., kinetic energy or acceleration) in a target reservoir, while undesired metrics (e.g., vibrational disturbance) in the surrounding neighborhood is minimized. The reservoir formation is discretized by using finite elements, surrounded by perfectly-matched-layers (PMLs) to truncate the semi-infinite extent of the reservoir domain (Kang and Kallivokas, 2010; Kucukcoban and Kallivokas, 2011, 2013). The PML is a buffer zone

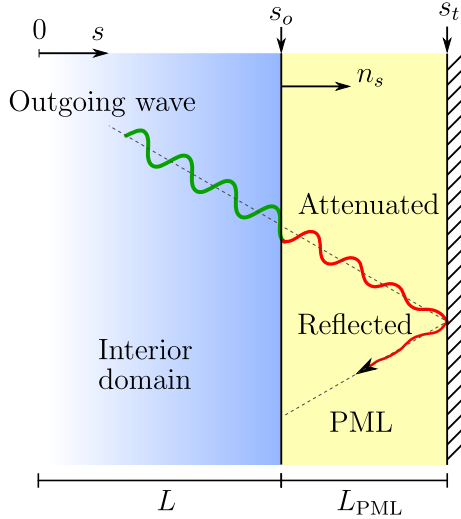


Fig. 3. A PML truncation boundary in the direction of coordinate s .

that surrounds the domain of interest, and forces the decay of both propagating and evanescent waves as they travel through the PML (Kucukcoban and Kallivokas, 2013; Fathi et al., 2015). This concept is schematically captured in Fig. 3.

The apparatus of PDE-constrained optimization is used to tackle the associated minimization problem. We report on numerical experiments, inverting for the optimal loading time signals that maximize the kinetic energy, or the acceleration field, within a synthetic reservoir inclusion.

2. Problem definition

A key objective is to identify the unknown loading signal characteristics of surface wave sources, which can maximize a desired motion metric, such as the kinetic energy, or acceleration field of the rock matrix, within a target reservoir formation, while also minimizing the disturbance of neighboring formations. In this section, the underlying elastic wave equations, which are coupled with PMLs in order to reduce the size of the computational domain, are discussed. We then introduce candidate objective functionals for optimizing the wave sources, and, finally, we discuss source parameterization.

2.1. Governing wave physics

We consider a target inclusion Ω_0 , embedded in a heterogeneous elastic solid medium of semi-infinite extent, subjected to multiple dynamic strip loadings, located on the ground surface, as shown in Fig. 4. In this figure, the target elastic inclusion Ω_0 , as well as the exterior domain $\Omega \setminus \Omega_0$ are occupied by a linear elastic solid. The semi-infinite extent of the elastic medium is negotiated by a buffer of Perfectly-Matched-Layers (PMLs) (Kucukcoban and Kallivokas, 2011, 2013), denoted by Ω_{PML} , placed at the domain's truncation boundary. Moreover, Ω_{reg} denotes the regular domain, which encompasses the entire domain excluding Ω_{PML} ($\Omega = \Omega_{\text{reg}} \cup \Omega_{\text{PML}}$). We adopt plane strain assumptions; i.e., spatially, the wave motion depends only on x_1 and x_2 . Accordingly, P-, SV-, and Rayleigh waves will be generated within Ω_{reg} . The elastic wave response is then governed by the following set of equations:

$$\text{div} \left(\frac{\partial \mathbf{S}_a^T}{\partial t} \right) - \rho \frac{\partial^2 \mathbf{u}_a}{\partial t^2} = \mathbf{0}, \quad \mathbf{x} \in \Omega_0, \quad t \in (0, T], \quad (1)$$

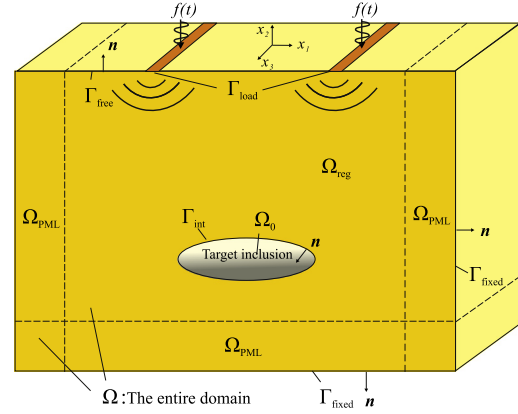


Fig. 4. The problem definition: identification of the loading time signal of the surface wave sources that can maximize the movement in the target inclusion Ω_0 embedded in the semi-infinite medium.

$$\mathcal{D} \left[\frac{\partial^2 \mathbf{S}_a}{\partial t^2} \right] - \frac{1}{2} \left[\nabla \frac{\partial \mathbf{u}_a}{\partial t} + \left(\nabla \frac{\partial \mathbf{u}_a}{\partial t} \right)^T \right] = \mathbf{0}, \quad \mathbf{x} \in \Omega_0, \quad t \in (0, T], \quad (2)$$

and

$$\text{div} \left(\frac{\partial \mathbf{S}_b^T}{\partial t} \tilde{\Lambda}_e + \mathbf{S}_b^T \tilde{\Lambda}_p \right) - \rho \left(a \frac{\partial^2 \mathbf{u}_b}{\partial t^2} + b \frac{\partial \mathbf{u}_b}{\partial t} + c \mathbf{u}_b \right) = \mathbf{0}, \quad \mathbf{x} \in \Omega \setminus \Omega_0, \quad t \in (0, T], \quad (3)$$

$$\begin{aligned} & \Lambda_e^T \left(\mathcal{D} \left[\frac{\partial^2 \mathbf{S}_b}{\partial t^2} \right] \right) \Lambda_e + \Lambda_e^T \left(\mathcal{D} \left[\frac{\partial \mathbf{S}_b}{\partial t} \right] \right) \Lambda_p \\ & + \Lambda_p^T \left(\mathcal{D} \left[\frac{\partial \mathbf{S}_b}{\partial t} \right] \right) \Lambda_e + \Lambda_p^T \left(\mathcal{D} \left[\mathbf{S}_b \right] \right) \Lambda_p \\ & - \frac{1}{2} \left[\Lambda_p^T \nabla \mathbf{u}_b + (\nabla \mathbf{u}_b)^T \Lambda_p \right] - \frac{1}{2} \left[\Lambda_e^T \nabla \frac{\partial \mathbf{u}_b}{\partial t} + \left(\nabla \frac{\partial \mathbf{u}_b}{\partial t} \right)^T \Lambda_e \right] = \mathbf{0}, \end{aligned} \quad \mathbf{x} \in \Omega \setminus \Omega_0, \quad t \in (0, T]. \quad (4)$$

The system is initially at rest, and subject to the following boundary and interface conditions:

$$\mathbf{u}_b(\mathbf{x}, t) = \mathbf{0}, \quad \mathbf{x} \in \Gamma_{\text{fixed}}, \quad (5a)$$

$$\frac{\partial \mathbf{S}_b^T(\mathbf{x}, t)}{\partial t} \mathbf{n}(\mathbf{x}) = \mathbf{f}(\mathbf{x}, t), \quad \mathbf{x} \in \Gamma_{\text{load}}, \quad (5b)$$

$$\left(\frac{\partial \mathbf{S}_b^T(\mathbf{x}, t)}{\partial t} \tilde{\Lambda}_e(\mathbf{x}) + \mathbf{S}_b^T(\mathbf{x}, t) \tilde{\Lambda}_p(\mathbf{x}) \right) \mathbf{n}(\mathbf{x}) = \mathbf{0}, \quad \mathbf{x} \in \Gamma_{\text{free}} \setminus \Gamma_{\text{load}}, \quad (5c)$$

$$\mathbf{u}_a(\mathbf{x}, t) = \mathbf{u}_b(\mathbf{x}, t), \quad \mathbf{x} \in \Gamma_{\text{int}}, \quad (6a)$$

$$\frac{\partial \mathbf{S}_a^T(\mathbf{x}, t)}{\partial t} \mathbf{n}(\mathbf{x}) = \frac{\partial \mathbf{S}_b^T(\mathbf{x}, t)}{\partial t} \mathbf{n}(\mathbf{x}), \quad \mathbf{x} \in \Gamma_{\text{int}}, \quad (6b)$$

where spatial and temporal dependencies are suppressed for brevity; \mathbf{u} is the displacement vector, $\partial \mathbf{S} / \partial t$ represents the Cauchy stress tensor, \mathcal{D} is the fourth-order compliance tensor, ρ is the mass density of the elastic solid medium, $\mathbf{x} = (x_1, x_2)^T$ denotes space, t is time, T represents the total observation time, \mathbf{n} is the unit outward normal vector at the interface boundaries, $\mathbf{f} = (f_1, f_2)^T$ is the vector of external forces, yet to be determined,¹ and subscripts 'a' and 'b' represent variables in Ω_0 and $\Omega \setminus \Omega_0$, respectively. Moreover, $\tilde{\Lambda}_e$, $\tilde{\Lambda}_p$, Λ_e , and Λ_p are the so-called stretch tensors, which enforce attenuation of waves within the PML, and a , b , and c are products of certain elements of the stretch tensors (Kucukcoban and Kallivokas, 2011, 2013).

¹ Throughout, we only consider vertical excitations, i.e., $f_1 \equiv 0$.

Eqs. (1) and (2) are the equilibrium and the combined constitutive and kinematic equations in the target reservoir Ω_0 ,² respectively. Eqs. (3) and (4) are the equilibrium and the combined constitutive and kinematic equations in the surrounding elastic solid medium $\Omega \setminus \Omega_0$, which also includes Ω_{PML} . These equations are coupled via (6a) and (6b), which are the continuity of displacements and traction conditions at Γ_{int} , respectively. We remark that in (1)–(4) the displacement field and the stress history tensor are both treated as unknowns, resulting in a mixed formulation.

2.2. Candidate objective functionals

Considering the problem configuration, we seek to identify the loading time signals of the wave sources that, for example, can maximize the kinetic energy in a target inclusion Ω_0 . This can be realized by minimizing the following objective functional:

$$\mathcal{L} = \frac{1}{\int_{\Omega_0} \int_0^T \rho \left[\left(\frac{\partial u_{a_1}}{\partial t} \right)^2 + \left(\frac{\partial u_{a_2}}{\partial t} \right)^2 \right] dt d\Omega} \quad (7)$$

Alternatively, one may aim at maximizing the kinetic energy in the target inclusion Ω_0 , while simultaneously minimizing the kinetic energy in the neighboring formations $\Omega_{\text{reg}} \setminus \Omega_0$. This can be accomplished by minimizing an objective functional of the form:

$$\mathcal{L} = \frac{\int_{\Omega_{\text{reg}} \setminus \Omega_0} \int_0^T \rho \left[\left(\frac{\partial u_{b_1}}{\partial t} \right)^2 + \left(\frac{\partial u_{b_2}}{\partial t} \right)^2 \right] dt d\Omega}{\int_{\Omega_0} \int_0^T \rho \left[\left(\frac{\partial u_{a_1}}{\partial t} \right)^2 + \left(\frac{\partial u_{a_2}}{\partial t} \right)^2 \right] dt d\Omega} \quad (8)$$

The denominators of (7) and (8) are the temporal integrals of the kinetic energy that is spatially integrated over Ω_0 ; the numerator of (8) is the temporal integral of the kinetic energy that is spatially integrated over the formations surrounding the reservoir $\Omega_{\text{reg}} \setminus \Omega_0$.

We remark that the form of the objective functional can be altered depending on the metric to be minimized or maximized. For instance, a different objective functional could be cast in terms of the acceleration field:

$$\mathcal{L} = \frac{1}{\int_{\Omega_0} \int_0^T \left[\left(\frac{\partial^2 u_{a_1}}{\partial t^2} \right)^2 + \left(\frac{\partial^2 u_{a_2}}{\partial t^2} \right)^2 \right] dt d\Omega} \quad (9)$$

Eq. (9) is the reciprocal of the temporal integral of the square of the amplitude of the acceleration field that is integrated over the target inclusion Ω_0 . Minimization of (9) can lead to optimal loading time signals that can maximize the rock matrix acceleration within Ω_0 .

The performance of each of these objective functionals is examined in Section 5, using various numerical experiments.

2.3. Load parameterization

We consider the loading time signal $f_2(t)$ to be unknown. The load can be parameterized as:

$$f_2(t) = \sum_{i=1}^{n_f} f_{2_i} \varphi_i(t), \quad (10)$$

where $\varphi_i(t)$ and f_{2_i} denote the i th (temporal) shape function and the discrete temporal excitation parameter, respectively, and n_f is the total number of the discretized force parameters; we use quadratic shape functions for $\varphi_i(t)$, as shown in Fig. 5. Our goal is

to compute optimal values for f_{2_i} , such that the resulting loading time signal minimizes the considered objective functional \mathcal{L} .

3. The inverse source problem

Our goal is to compute the temporal characteristics of the wave sources that are placed on the ground surface, such that the chosen objective functional is minimized. To this end, we first construct a Lagrangian functional \mathcal{A} by augmenting the objective functional with the side imposition of the governing wave equations. Specifically, we introduce Lagrange multiplier vector functions $\lambda_{u_a}(\mathbf{x}, t)$, $\lambda_{u_b}(\mathbf{x}, t)$, $\lambda_F(\mathbf{x}, t)$, and Lagrange multiplier tensor functions $\lambda_{S_a}(\mathbf{x}, t)$, $\lambda_{S_b}(\mathbf{x}, t)$ to enforce the initial- and boundary value problem (1)–(6). The Lagrangian functional becomes

$$\begin{aligned} \mathcal{A} = & \frac{1}{\int_{\Omega_0} \int_0^T \rho \left[\left(\frac{\partial u_{a_1}}{\partial t} \right)^2 + \left(\frac{\partial u_{a_2}}{\partial t} \right)^2 \right] dt d\Omega} \\ & + \int_{\Omega_0} \int_0^T \lambda_{u_a} \cdot \left[\mathbf{div} \left(\frac{\partial \mathbf{S}_a^T}{\partial t} \right) - \rho \frac{\partial^2 \mathbf{u}_a}{\partial t^2} \right] dt d\Omega \\ & + \int_{\Omega_0} \int_0^T \lambda_{S_a} : \left[\mathcal{D} \left[\frac{\partial^2 \mathbf{S}_a}{\partial t^2} \right] - \frac{1}{2} \left\{ \nabla \frac{\partial \mathbf{u}_a}{\partial t} + \left(\nabla \frac{\partial \mathbf{u}_a}{\partial t} \right)^T \right\} \right] dt d\Omega \\ & + \int_{\Omega \setminus \Omega_0} \int_0^T \lambda_{u_b} \cdot \left[\mathbf{div} \left(\frac{\partial \mathbf{S}_b^T}{\partial t} \tilde{\Lambda}_e + \mathbf{S}_b^T \tilde{\Lambda}_p \right) \right. \\ & \quad \left. - \rho \left(a \frac{\partial^2 \mathbf{u}_b}{\partial t^2} + b \frac{\partial \mathbf{u}_a}{\partial t} + c \mathbf{u}_b \right) \right] dt d\Omega \\ & + \int_{\Omega \setminus \Omega_0} \int_0^T \lambda_{S_b} : \left[\Lambda_e^T \left(\mathcal{D} \left[\frac{\partial^2 \mathbf{S}_b}{\partial t^2} \right] \right) \Lambda_e + \Lambda_e^T \left(\mathcal{D} \left[\frac{\partial \mathbf{S}_b}{\partial t} \right] \right) \Lambda_p \right. \\ & \quad \left. + \Lambda_p^T \left(\mathcal{D} \left[\frac{\partial \mathbf{S}_b}{\partial t} \right] \right) \Lambda_e + \Lambda_p^T \left(\mathcal{D} [\mathbf{S}_b] \right) \Lambda_p \right. \\ & \quad \left. - \frac{1}{2} \left\{ \Lambda_p^T \nabla \mathbf{u}_b + (\nabla \mathbf{u}_b)^T \Lambda_p \right\} \right. \\ & \quad \left. - \frac{1}{2} \left\{ \Lambda_e^T \nabla \frac{\partial \mathbf{u}_b}{\partial t} + \left(\nabla \frac{\partial \mathbf{u}_b}{\partial t} \right)^T \Lambda_e \right\} \right] dt d\Omega \\ & + \int_{\Gamma_{\text{load}}} \int_0^T \lambda_F \cdot \left[\frac{\partial \mathbf{S}_b^T}{\partial t} \mathbf{n} - \mathbf{f}(\mathbf{x}, t) \right] dt d\Gamma, \quad (11) \end{aligned}$$

where (\cdot) and $(:)$ indicate inner-product for vector- and tensor-variables, respectively. Moreover, (5a), (5c), (6), and the initial conditions, are implicitly considered in the Lagrangian \mathcal{A} .

Next, we use the Lagrangian (11) to compute the first-order optimality conditions. To this end, variation of \mathcal{A} with respect to the state variables $(\mathbf{u}_a, \mathbf{u}_b, \mathbf{S}_a, \mathbf{S}_b)$, the adjoint variables $(\lambda_{u_a}, \lambda_{u_b}, \lambda_{S_a}, \lambda_{S_b}, \lambda_F)$, and the control variables (f_{2_i}) – these are the sought temporal source parameters – must vanish.

3.1. The state problem

Taking the variation of the Lagrangian functional \mathcal{A} with respect to the adjoint variables $\lambda_{u_a}, \lambda_{u_b}, \lambda_{S_a}, \lambda_{S_b}, \lambda_F$,³ and setting it to zero, i.e., $\delta_{\lambda} \mathcal{A} = 0$, results in the state problem, which is identical to the forward problem, outlined in (1)–(6).

3.2. The adjoint problem

Taking the variation of \mathcal{A} with respect to the state variables $\mathbf{u}_a, \mathbf{u}_b, \mathbf{S}_a, \mathbf{S}_b$,⁴ and setting it to zero ($\delta_{u,S} \mathcal{A} = 0$), results in the adjoint

² In a more realistic setting, these equations can be replaced by Biot's equations (Biot, 1956), to represent a fluid-saturated porous permeable medium.

³ The variations of the adjoint variables are denoted by $\delta \lambda_{u_a}, \delta \lambda_{u_b}, \delta \lambda_{S_a}, \delta \lambda_{S_b}, \delta \lambda_F$.

⁴ The variations of the state variables are denoted by $\delta \mathbf{u}_a, \delta \mathbf{u}_b, \delta \mathbf{S}_a, \delta \mathbf{S}_b$.

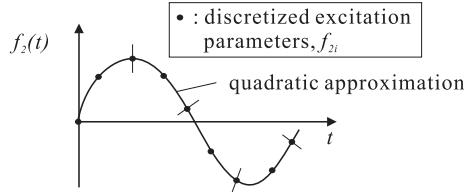


Fig. 5. Schematic of parameterization of an unknown excitation $f_2(t)$ using quadratic shape functions.

problem:

$$\frac{\partial^2 \lambda_{u_a}}{\partial t^2} \rho + \mathbf{div} \left(\frac{\partial \lambda_{S_a}^{\text{sym}}}{\partial t} \right) = \rho \mathcal{E} \frac{\partial^2 \mathbf{u}_a}{\partial t^2}, \quad \mathbf{x} \in \Omega_0, \quad t \in [0, T), \quad (12)$$

$$\mathcal{D} \left[\frac{\partial^2 \lambda_{S_a}^{\text{sym}}}{\partial t^2} \right] + \frac{1}{2} \left[\nabla \frac{\partial \lambda_{u_a}}{\partial t} + \left(\nabla \frac{\partial \lambda_{u_a}}{\partial t} \right)^T \right] = \mathbf{0}, \quad \mathbf{x} \in \Omega_0, \quad t \in [0, T), \quad (13)$$

$$\frac{\partial^2 \lambda_{u_b}}{\partial t^2} \rho a - \frac{\partial \lambda_{u_b}}{\partial t} \rho b + \lambda_{u_b} \rho c + \mathbf{div} \left(-\Lambda_p \lambda_{S_b}^{\text{sym}} + \Lambda_e \frac{\partial \lambda_{S_b}^{\text{sym}}}{\partial t} \right) = \rho \mathcal{E} \frac{\partial^2 \mathbf{u}_b}{\partial t^2}, \quad \mathbf{x} \in \Omega \setminus \Omega_0, \quad t \in [0, T), \quad (14)$$

$$\begin{aligned} & \frac{1}{2} \left[\tilde{\Lambda}_e \left(\nabla \frac{\partial \lambda_{u_b}}{\partial t} \right)^T + \left(\nabla \frac{\partial \lambda_{u_b}}{\partial t} \right) \tilde{\Lambda}_e \right] - \frac{1}{2} \left[\tilde{\Lambda}_p (\nabla \lambda_{u_b})^T + (\nabla \lambda_{u_b}) \tilde{\Lambda}_p \right] \\ & + \mathcal{D} \left[\Lambda_e^T \frac{\partial^2 \lambda_{S_b}^{\text{sym}}}{\partial t^2} - \Lambda_e - \Lambda_e^T \frac{\partial \lambda_{S_b}^{\text{sym}}}{\partial t} - \Lambda_p - \Lambda_p^T \frac{\partial \lambda_{S_b}^{\text{sym}}}{\partial t} - \Lambda_e + \Lambda_p^T \lambda_{S_b}^{\text{sym}} \Lambda_p \right] = \mathbf{0}, \\ & \mathbf{x} \in \Omega \setminus \Omega_0, \quad t \in [0, T), \end{aligned} \quad (15)$$

where $\lambda_{S_a}^{\text{sym}}$ and $\lambda_{S_b}^{\text{sym}}$ denote the symmetric part of λ_{S_a} and λ_{S_b} , respectively. That is, $\lambda_{S_a}^{\text{sym}} = \frac{1}{2}(\lambda_{S_a} + \lambda_{S_a}^T)$, and $\lambda_{S_b}^{\text{sym}} = \frac{1}{2}(\lambda_{S_b} + \lambda_{S_b}^T)$. Moreover, the coefficient $\mathcal{E}(\mathbf{x})$ in the body force term in (12) and (14) is defined as

$$\mathcal{E}(\mathbf{x}) = \begin{cases} \frac{2}{\left(\int_{\Omega_0} \int_0^T \rho \left[\frac{\partial \mathbf{u}_a}{\partial t} \cdot \frac{\partial \mathbf{u}_a}{\partial t} \right] dt d\Omega \right)^2}, & \mathbf{x} \in \Omega_0, \\ 0, & \mathbf{x} \in \Omega \setminus \Omega_0 \end{cases} \quad (16)$$

The adjoint equations (12)–(15) are supplemented with the following boundary conditions:

$$\left(-\Lambda_p \lambda_{S_b}^{\text{sym}} + \Lambda_e \frac{\partial \lambda_{S_b}^{\text{sym}}}{\partial t} \right) \mathbf{n} = \mathbf{0}, \quad \mathbf{x} \in \Gamma_{\text{free}}, \quad (17a)$$

$$\lambda_{u_b} = \mathbf{0}, \quad \mathbf{x} \in \Gamma_{\text{fixed}}, \quad (17b)$$

$$\lambda_F = -\lambda_{u_b}, \quad \mathbf{x} \in \Gamma_{\text{load}}, \quad (17c)$$

interface conditions:

$$\lambda_{u_a} = \lambda_{u_b}, \quad \lambda_{S_a} \mathbf{n} = \lambda_{S_b} \mathbf{n}, \quad \mathbf{x} \in \Gamma_{\text{int}}, \quad (18)$$

and, final value conditions:

$$\lambda_{u_a} = \mathbf{0}, \quad \frac{\partial \lambda_{u_a}}{\partial t} = \mathcal{E} \frac{\partial \mathbf{u}_a}{\partial t}, \quad \lambda_{S_a}^{\text{sym}} = \mathbf{0}, \quad \frac{\partial \lambda_{S_a}^{\text{sym}}}{\partial t} = \mathbf{0}, \quad \mathbf{x} \in \Omega_0, \quad t = T, \quad (19a)$$

$$\lambda_{u_b} = \mathbf{0}, \quad \frac{\partial \lambda_{u_b}}{\partial t} = \mathcal{E} \frac{\partial \mathbf{u}_b}{\partial t}, \quad \lambda_{S_b}^{\text{sym}} = \mathbf{0}, \quad \frac{\partial \lambda_{S_b}^{\text{sym}}}{\partial t} = \mathbf{0}, \quad \mathbf{x} \in \Omega \setminus \Omega_0, \quad t = T. \quad (19b)$$

We remark that the adjoint problem is a final value problem, and, thus, is solved backwards in time; it is driven by body force terms $\rho \mathcal{E}(\partial^2 \mathbf{u}_a / \partial t^2)$, $\rho \mathcal{E}(\partial^2 \mathbf{u}_b / \partial t^2)$, which are obtained from solving the state problem. Moreover, we remark that the operators implicated in the adjoint problem are very similar to those in

the forward problem (modulo sign reversals associated with odd-order time derivatives). Thus, an implementation of the forward problem can be used for the resolution of the adjoint problem, with only minor modifications.

If the objective functional shown in (8) – the silent neighboring formations – is minimized, the adjoint problem remains overall unaltered, except that the coefficient $\mathcal{E}(\mathbf{x})$ is modified to read:

$$\mathcal{E}(\mathbf{x}) = \begin{cases} \frac{2 \left(\int_{\Omega_{\text{reg}} \setminus \Omega_0} \int_0^T \rho \left[\frac{\partial \mathbf{u}_b}{\partial t} \cdot \frac{\partial \mathbf{u}_b}{\partial t} \right] dt d\Omega \right)}{\left(\int_{\Omega_0} \int_0^T \rho \left[\frac{\partial \mathbf{u}_a}{\partial t} \cdot \frac{\partial \mathbf{u}_a}{\partial t} \right] dt d\Omega \right)^2}, & \mathbf{x} \in \Omega_0, \\ -2 \frac{\left(\int_{\Omega_0} \int_0^T \rho \left[\frac{\partial \mathbf{u}_a}{\partial t} \cdot \frac{\partial \mathbf{u}_a}{\partial t} \right] dt d\Omega \right)}{\left(\int_{\Omega_0} \int_0^T \rho \left[\frac{\partial \mathbf{u}_a}{\partial t} \cdot \frac{\partial \mathbf{u}_a}{\partial t} \right] dt d\Omega \right)}, & \mathbf{x} \in \Omega_{\text{reg}} \setminus \Omega_0, \\ 0, & \mathbf{x} \in \Omega \setminus \Omega_{\text{reg}} \end{cases} \quad (20)$$

If the acceleration-based objective functional (9), is used instead, then the adjoint equations change as follows: firstly, Eqs. (12) and (14) are, respectively, replaced by

$$\frac{\partial^2 \lambda_{u_a}}{\partial t^2} \rho + \mathbf{div} \left(\frac{\partial \lambda_{S_a}^{\text{sym}}}{\partial t} \right) = -\mathcal{E} \frac{\partial^4 \mathbf{u}_a}{\partial t^4}, \quad \mathbf{x} \in \Omega_0, \quad t \in [0, T), \quad (21)$$

$$\frac{\partial^2 \lambda_{u_b}}{\partial t^2} \rho a - \frac{\partial \lambda_{u_b}}{\partial t} \rho b + \lambda_{u_b} \rho c + \mathbf{div} \left(-\Lambda_p \lambda_{S_b}^{\text{sym}} + \Lambda_e \frac{\partial \lambda_{S_b}^{\text{sym}}}{\partial t} \right) = -\mathcal{E} \frac{\partial^4 \mathbf{u}_b}{\partial t^4}, \quad \mathbf{x} \in \Omega \setminus \Omega_0, \quad t \in [0, T), \quad (22)$$

whereas the other adjoint PDEs, (13) and (15), remain unaltered. We remark that, in (21) and (22), the right-hand-side body force terms include the fourth derivative of the state solution with respect to time t , as well as a modified coefficient $\mathcal{E}(\mathbf{x})$, which is defined as

$$\mathcal{E}(\mathbf{x}) = \begin{cases} \frac{2}{\left(\int_{\Omega_0} \int_0^T \rho \left[\frac{\partial^2 \mathbf{u}_a}{\partial t^2} \cdot \frac{\partial^2 \mathbf{u}_a}{\partial t^2} \right] dt d\Omega \right)^2}, & \mathbf{x} \in \Omega_0, \\ 0, & \mathbf{x} \in \Omega \setminus \Omega_0 \end{cases} \quad (23)$$

Secondly, the final value conditions (19) are replaced by

$$\lambda_{u_a} = -\frac{\mathcal{E}}{\rho} \frac{\partial^2 \mathbf{u}_a}{\partial t^2}, \quad \frac{\partial \lambda_{u_a}}{\partial t} = -\frac{\mathcal{E}}{\rho} \frac{\partial^3 \mathbf{u}_a}{\partial t^3}, \quad \lambda_{S_a}^{\text{sym}} = \mathbf{0}, \quad \frac{\partial \lambda_{S_a}^{\text{sym}}}{\partial t} = \mathbf{0}, \quad \mathbf{x} \in \Omega_0, \quad t = T, \quad (24a)$$

$$\lambda_{u_b} = -\frac{\mathcal{E}}{\rho a} \frac{\partial^2 \mathbf{u}_b}{\partial t^2}, \quad \frac{\partial \lambda_{u_b}}{\partial t} = -\frac{\mathcal{E}}{\rho a} \frac{\partial^3 \mathbf{u}_b}{\partial t^3} - \frac{\mathcal{E} b}{\rho a^2} \frac{\partial^2 \mathbf{u}_b}{\partial t^2}, \quad \lambda_{S_b}^{\text{sym}} = \mathbf{0}, \quad \frac{\partial \lambda_{S_b}^{\text{sym}}}{\partial t} = \mathbf{0}, \quad \mathbf{x} \in \Omega \setminus \Omega_0, \quad t = T. \quad (24b)$$

3.3. The control problem

The third optimality condition requires $\delta_{f_{2i}} \mathcal{A} = 0$, i.e., the vanishing variation of \mathcal{A} with respect to the control parameters f_{2i} , which parameterize the load $f_2(t)$, as detailed in (10). This yields

$$\delta_{f_{2i}} \mathcal{A} = \int_{\Gamma_{\text{load}}} \int_0^T \left[\lambda_{u_2}(\mathbf{x}, t) \frac{\partial f_2(t)}{\partial f_{2i}} \right] dt d\Gamma = 0. \quad (25)$$

Moreover $\delta_{f_{2i}} \mathcal{A} = \nabla_{f_{2i}} \mathcal{A}$.

We remark that in the reduced-space approach detailed in the next section, the gradient of the augmented functional \mathcal{A} equals the gradient of the objective functional \mathcal{L} , since the side-imposed constraints of the augmented functional \mathcal{A} vanish, owing to the

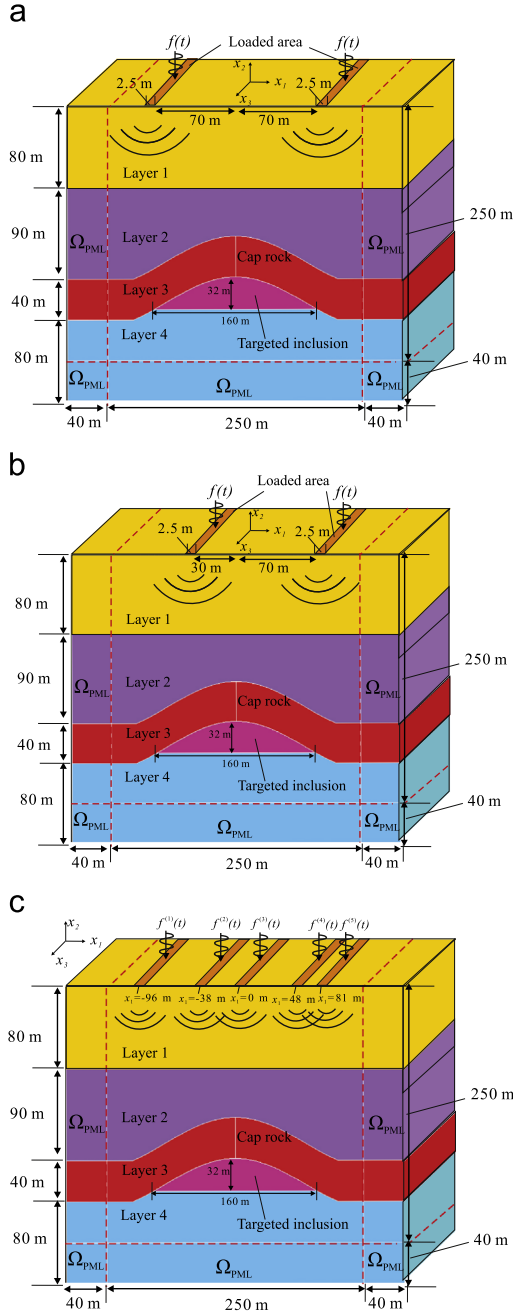


Fig. 6. Subsurface formation model – a target hydrocarbon reservoir inclusion Ω_0 buried in a semi-infinite heterogeneous medium subjected to various ground wave sources: (a) two symmetric wave sources, (b) two unsymmetric wave sources, and (c) five unsymmetric wave sources.

satisfaction of the state problem. That is,

$$\nabla_{f_{2i}} \mathcal{L} = \int_{\Gamma_{\text{load}}} \int_0^T [\lambda_{u_2}(\mathbf{x}, t) \varphi_i(t)] dt d\Gamma. \quad (26)$$

Thus, with the aid of this gradient, a gradient-based scheme can be employed to minimize the objective functional \mathcal{L} .

4. The inversion process

In this non-linear minimization problem, we iteratively identify a stationary point by using a gradient-based minimization approach until the first-order optimality conditions – the triplet of the state, adjoint, and control equations – are satisfied. The iterative procedure

Table 1

Elastic moduli and wave velocities of the layers of the model shown in Fig. 6.

Formation	E (N/m ²)	v_p (m/s)	v_s (m/s)
Target	1.0×10^{10}	2247	1376
Layer 1	2.0×10^{10}	3178	1946
Layer 2	2.4×10^{10}	3482	2132
Layer 3	3.0×10^{10}	3892	2384
Layer 4	3.6×10^{10}	4264	2611

undergoes the following steps: (a) the state problem, shown in Eqs. (1)–(6), is solved by using an initially guessed loading time signal; (b) the adjoint problem, shown in (12)–(19), is subsequently solved by using the state solution; (c) the gradient $\nabla_{f_{2i}} \mathcal{L}$, as shown in (26), is evaluated; and (d) the control parameters f_{2i} are updated by virtue of a conjugate-gradient (CG) scheme (Fletcher and Reeves, 1951; Nocedal and Wright, 2006) with an inexact line-search method (Nocedal and Wright, 2006). The numerical optimizer repeats steps (a)–(d) until the control parameters converge. The numerical optimization scheme is summarized in Algorithm 1. Herein, a standard Galerkin method is used to solve the state and adjoint problems.

The accuracy of the PML in the forward wave solver was verified via comparison with a reference solution for an enlarged domain with fixed boundaries (Kucukcoban, 2010; Kucukcoban and Kallivokas, 2011, 2013). We also verified the mathematical derivation and numerical implementation of the trio of the state, adjoint, and control problems by comparing (i) the values of the components of the gradient computed by (26) using a set of arbitrary force parameters with (ii) those of the numerical gradient obtained by a finite-difference scheme, which is straightforward but computationally expensive, as

$$\nabla_{f_{2i}} \mathcal{L} = \frac{\mathcal{L}|_{f_{2i} + \Delta f_{2i}} - \mathcal{L}|_{f_{2i} - \Delta f_{2i}}}{2\Delta f_{2i}}, \quad (27)$$

where $\mathcal{L}|_{f_{2i} + \Delta f_{2i}}$ (or $\mathcal{L}|_{f_{2i} - \Delta f_{2i}}$) denotes the value of \mathcal{L} evaluated for the same given set of force parameters whose i th parameter is increased by Δf_{2i} from the original value (or decreased by Δf_{2i}); Δf_{2i} denotes the incremental step size used for the finite-difference scheme. Both gradients (the control (26) versus the finite-difference (27)) yield identical numerical values.

Algorithm 1. Optimization algorithm.

- 1: Set Tol = 10^{-8} , $\alpha = 0.9$ and $\beta = 1.1$
- 2: Set $k=0$, and initialize force parameters $\mathbf{f}_{(0)}$
- 3: Compute $\mathcal{L}_{(k)}$
- 4: **while** ($e > \text{Tol}$) **do**
- 5: Solve the state problem and store the state variables
- 6: Solve the adjoint problem and store the adjoint variables
- 7: Compute a search-direction \mathbf{g} by using CG
- 8: **while** ($\mathcal{L}(\mathbf{f}_{(k)} + \theta_{(k)} \mathbf{g}) > \mathcal{L}(\mathbf{f}_{(k)} - \frac{1}{2} \theta_{(k)} \nabla \mathcal{L}(\mathbf{f}_{(k)}))$) **do**
- 9: $\theta_{(k)} \leftarrow \alpha \theta_{(k)}$
- 10: **end while**
- 11: Update excitation parameters $\mathbf{f}_{(k+1)}$, and compute $\mathcal{L}_{(k+1)}$
- 12: Compute the termination condition: $e = \frac{|\mathcal{L}_{(k+1)} - \mathcal{L}_{(k)}|}{|\mathcal{L}_{(k)}|}$
- 13: $\theta_{(k+1)} \leftarrow \beta \theta_{(k)}$, and $k \leftarrow k+1$
- 14: **end while**

5. Numerical experiments

We present numerical experiments conducted for a synthetic subsurface formation model (Fig. 6), which comprises 4 layers and a

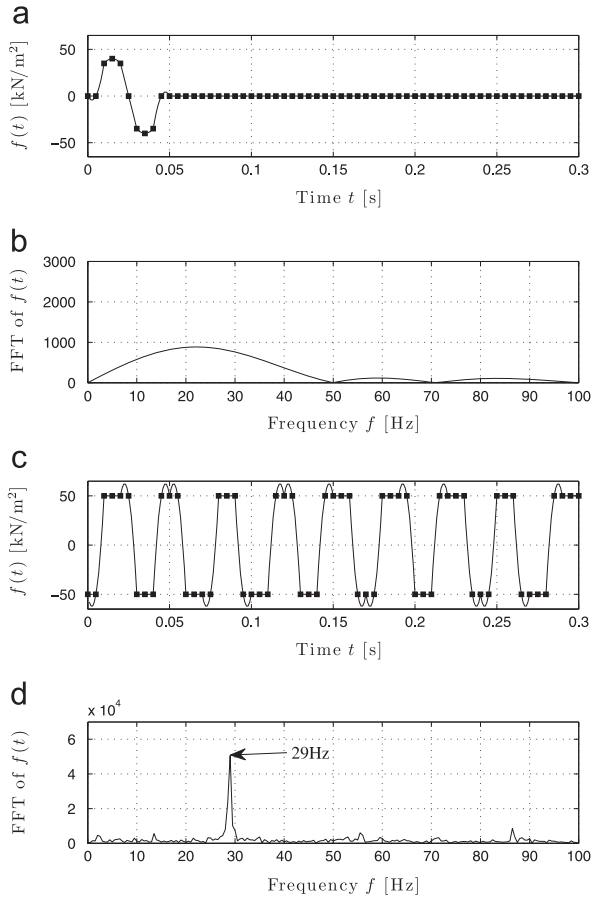


Fig. 7. The initially guessed and optimized loading signals for the maximization of the kinetic energy in Ω_0 of the formation model shown in Fig. 6(a) (minimizing (7)): (a) close-up view (0–0.3 s) of the initially guessed signal, (b) the frequency spectrum of the initially guessed signal, (c) close-up view (0–0.3 s) of the converged signal, and (d) the frequency spectrum of the converged signal.

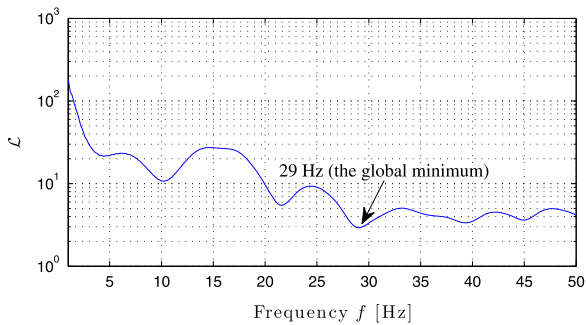


Fig. 8. Frequency sweep of the objective functional, (7), using a harmonic load $f_2(t) = 50 \sin(2\pi ft)$ kN/m² for the formation model shown in Fig. 6(a).

target oil reservoir inclusion embedded between the third and fourth layers. The width and height of the target reservoir inclusion are 160 m and 32 m, respectively; the distance from the ground surface to the bottom of the inclusion is 200 m. This dome-shaped inclusion exemplifies a typical shallow oil reservoir structure underneath an impermeable curved cap stratum. The figures (a), (b), and (c) in Fig. 6 differ from each other only with respect to the location of the wave sources.

In this example, it is assumed that the elastic modulus E for each layer becomes larger as the depth increases, and the inclusion

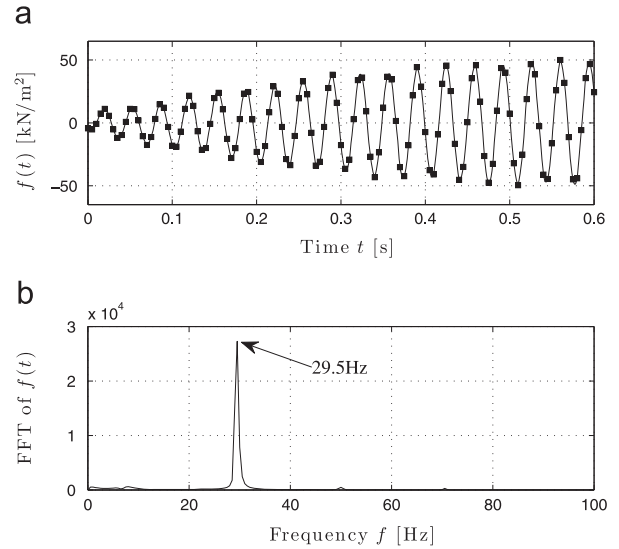


Fig. 9. Converged loading time signal for the maximization of the kinetic energy in Ω_0 with silent neighbors for formation model shown in Fig. 6(a): (a) close-up view (0–0.5 s) of the converged signal and (b) the frequency spectrum of the converged signal.

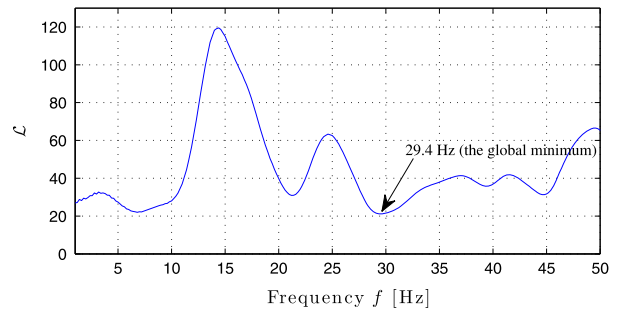


Fig. 10. Frequency sweep of the objective functional, (8), using a harmonic load $f_2(t) = 50 \sin(2\pi ft)$ kN/m² for the formation model shown in Fig. 6(a).

is softer than the surrounding layers.⁵ We set the mass density $\rho = 2200$ kg/m³ and Poisson's ratio $\nu = 0.2$. Then, using the above values for E , ρ , and ν , the compressional wave velocity v_p and the shear wave velocity v_s of each area can be obtained as

$$v_p = \sqrt{\frac{\lambda + 2\mu}{\rho}} = \sqrt{\frac{E(1-\nu)}{\rho(1+\nu)(1-2\nu)}}, \quad v_s = \sqrt{\frac{\mu}{\rho}} = \sqrt{\frac{E}{2\rho(1+\nu)}}, \quad (28)$$

where λ denotes Lamé's first parameter and μ denotes shear modulus. The elastic moduli and wave velocities of the model are summarized in Table 1. In the following examples, isoparametric quadrilateral (or triangular) quadratic elements are used to discretize the state and adjoint problems. The size of the elements are approximately 4.0 m or less, in order to discretize with at least 12 points per wavelength: the minimum wavelength, corresponding to the highest frequency (50 Hz), in the area of the smallest shear wave velocity in this model is approximately 27.5 m.

5.1. Source optimization solutions

Numerical experiments are conducted for three different configurations of the wave sources: (1) two symmetric wave sources (Fig. 6(a)); (2) two independent unsymmetric wave sources (Fig. 6(b)); and (3) five independent unsymmetric wave sources (Fig. 6(c)). We considered

⁵ The poroelastic medium partially saturated with fluid or gas phases is generally softer than the surrounding media (Gassmann, 1951).

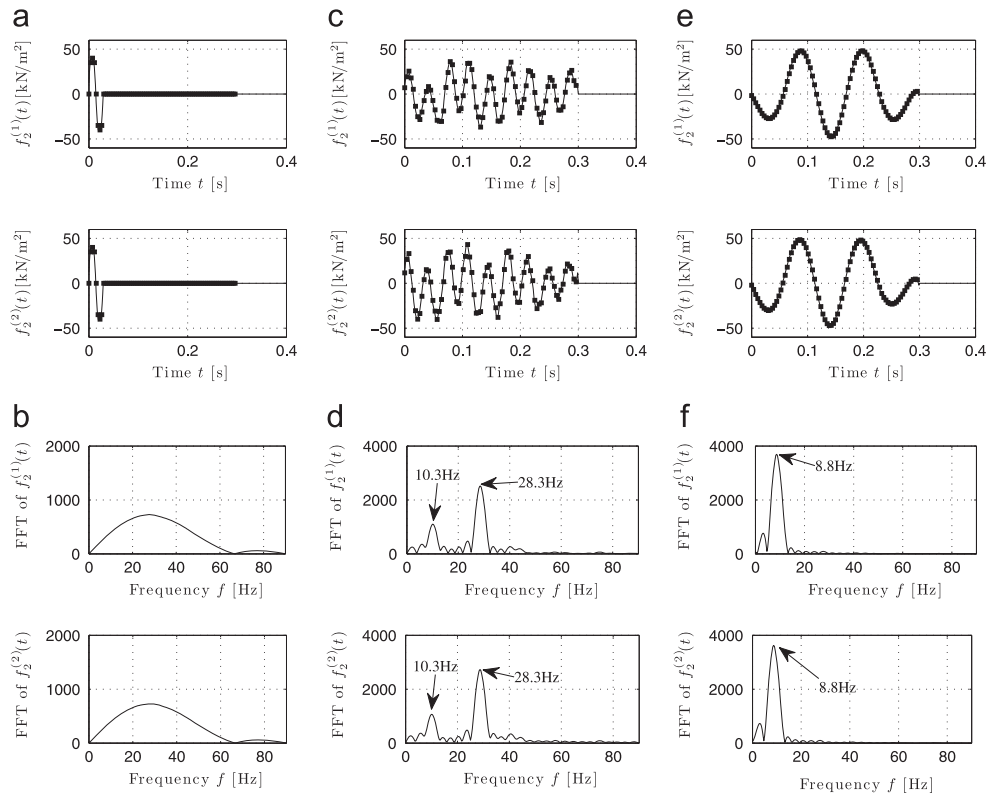


Fig. 11. Initial guesses and optimized loading signals for two independent wave sources at $x_1 = -30$ m and $x_1 = 70$ m corresponding to the maximization of the kinetic energy in Ω_0 with silent neighbors for the formation model in Fig. 6(b): (a) the initially guessed signals, (b) the frequency spectra of the initially guessed signals, (c) the optimized signals at the 36th iteration, (d) the frequency spectra of the optimized signals at the 36th iteration, (e) the finally converged signals, and (f) the frequency spectra of the finally converged signals.

three different objective functionals for optimization, that is, (A) maximization of the kinetic energy in Ω_0 with all layers active (i.e., minimization of functional (7)); (B) maximization of the kinetic energy in Ω_0 with silent neighbors (i.e., minimization of functional (8)); and (C) maximization of the acceleration in Ω_0 with all layers active (i.e., minimization of functional (9)). The results of these experiments are summarized in Table 4 using the optimization case numbers.⁶ A subset of the numerical experiments are described in detail next; namely, cases 1A, 1B, 2B, 3B, and 1C.

5.1.1. Two symmetric optimal wave sources for maximum kinetic energy in a target (case 1A)

We identify the optimal loading time signals for two symmetric wave sources (Fig. 6(a)), which can maximize the kinetic energy within the target inclusion Ω_0 . To this end, we seek to minimize (7) by using the initially guessed loading time signal, temporally discretized by 200 quadratic elements (400 discretized force parameters), shown in Fig. 7(a). Here, the loading signals of the two wave sources are set to be identical to each other. The block symbols of the close-up view of the initially guessed signal in Fig. 7(a) represent the discretized force parameters used for the temporal approximation of the loading time signal: such symbols are used in all similar plots. We numerically require that the amplitude of each discretized loading parameter, $f_{2,i}$, does not exceed 60 kN/m^2 (a modern Vibroseis can deliver dynamic pressure up to 60 kN/m^2 or more to the ground surface, Kalinski, 2007). The frequency spectrum of the initially guessed loading is shown in Fig. 7(b). The initially guessed signal

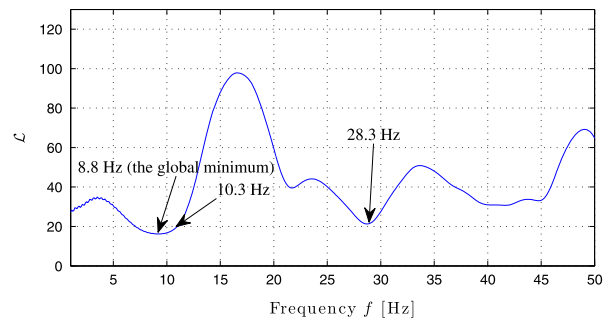


Fig. 12. Frequency sweep of the objective functional, (8), using a harmonic load $f_2(t) = 50 \sin(2\pi ft) \text{ kN/m}^2$ for the formation model shown in Fig. 6(b).

has a broad frequency spectrum, which, as it will be seen, differs significantly from that of the finally converged time signal: the optimization process is unbiased with respect to the initial guess. The total observation time is 2 s, and the time step is 0.001 s.

Fig. 7(c, d) shows that our numerical optimizer converges, after 66 iterations, to a loading time signal with a dominant frequency of 29 Hz. Fig. 8 shows that the dominant frequency 29 Hz corresponds to the global minimum of the distribution of the objective functional, shown in (7), with respect to the frequency f for a sinusoidal loading $f_2(t) = 50 \sin(2\pi f) \text{ kN/m}^2$ for the formation model subject to the two symmetric wave sources shown in Fig. 6(a). That is, the optimizer successfully recovered a nearly-monochromatic signal corresponding to one of the formation’s amplification frequencies.

As discussed in our one-dimensional work (Jeong et al., 2010), the maximization of the kinetic energy within a target inclusion with all layers active is likely to recover a rectangular-shaped loading time signal (see the close-up view in Fig. 7(c)). Such a rectangular-shaped

⁶ For instance, the case number 1A refers to the optimization conducted for the identification of loading time signals of 1: two symmetric wave sources, that can lead to A: maximization of the kinetic energy of rock matrix in Ω_0 with all layers active.

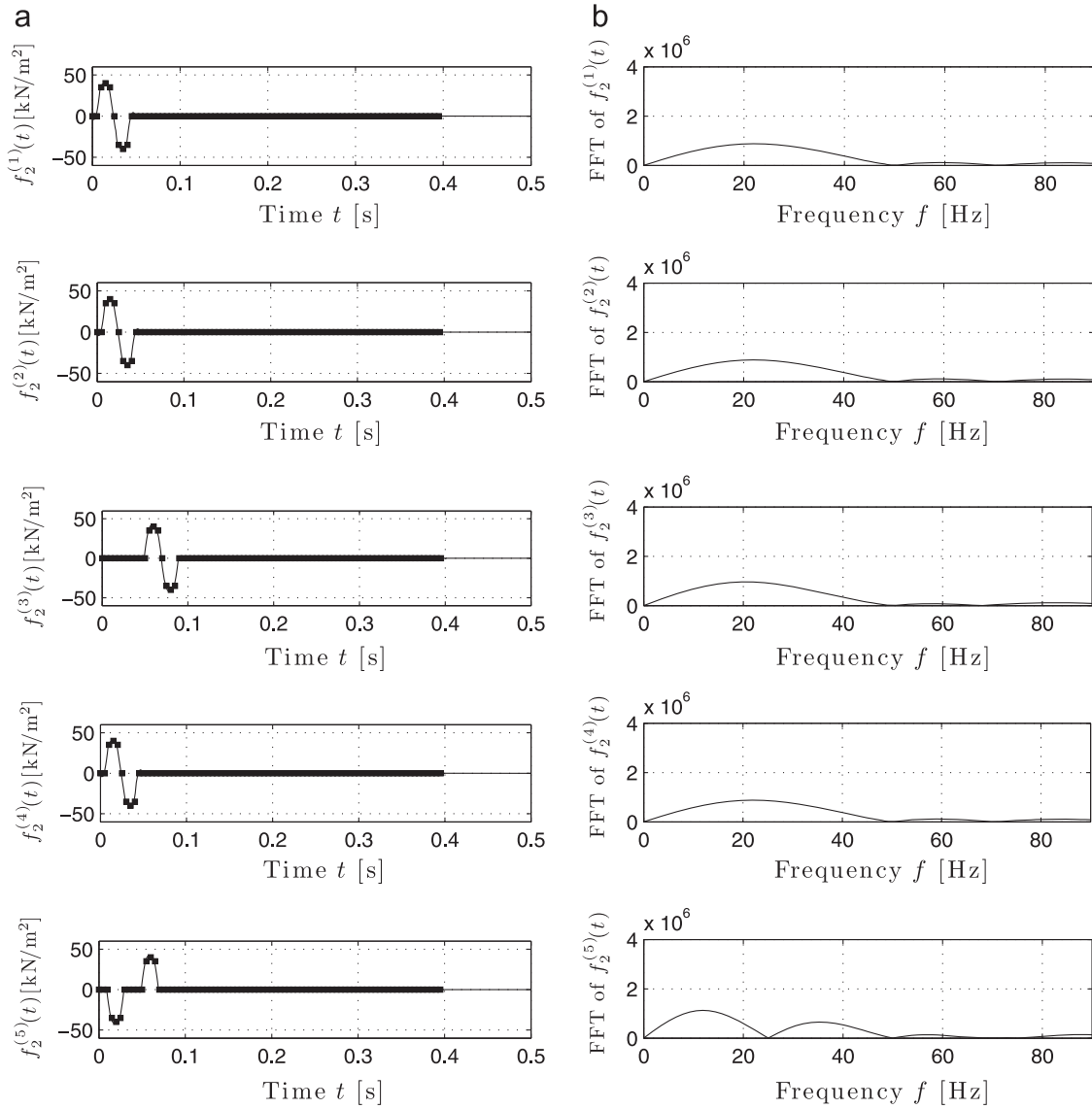


Fig. 13. The initially guessed loading time signals of the five wave sources at unsymmetric locations for the formation model shown in Fig. 6(c) for the maximization of the kinetic energy in Ω_0 with silent neighbors: (a) the initially guessed signals and (b) the frequency spectra of the initially guessed signals.

loading time signal contains a few high frequency components. Thus, the kinetic energy within Ω_0 for such a rectangular-shaped optimized loading time signal is larger than that of the monochromatic time signal $f_2(t) = 50 \sin(2\pi \times 29t)$ kN/m² that uses the dominant frequency of the rectangular-shaped signal (Fig. 18(a) vs (b)). Note that the kinetic energy distribution within Ω_0 for the converged time signal is much larger than that of a non-optimal sinusoidal loading $f_2(t) = 50 \sin(2\pi ft)$ kN/m² using a non-optimal frequency, such as $f = 25$ Hz (Fig. 18(a) vs (c)).

5.1.2. Two symmetric optimal wave sources for maximum kinetic energy in a target with silent neighbors (case 1B)

Next, we explore the possibility of maximizing the kinetic energy within Ω_0 while the kinetic energy within the surrounding areas $\Omega \setminus \Omega_0$ is minimized by considering the two symmetric wave sources displayed in Fig. 6(a). In particular, we aim to reduce the strong wave energy along the free surface via our optimization scheme by minimizing the objective functional (8).

The optimization process begins again with the initially guessed perturbation loading time signal that is temporally discretized by 200

quadratic elements (400 discretized force parameters); the total observation time is 2 s, and the time step is 0.001 s. After 71 iterations, the optimizer results in a sinusoidally shaped loading signal with a dominant frequency of 29.5 Hz (Fig. 9). This frequency corresponds to the global minimum of the objective functional (8), with respect to the frequency f for a sinusoidal loading $f_2(t) = 50 \sin(2\pi ft)$ kN/m², as shown in Fig. 10. Again, the optimizer successfully recovered one of the formation's amplification frequencies.

We point out that the recovered frequency of 29.5 Hz is quite close to the amplification frequency of 29 Hz, recovered in the previous experiment (all layers active). That is, the optimizer arrives at a stationary point for (8) largely due to maximizing the kinetic energy in the inclusion, rather than by minimizing the wave energy in the neighboring formations. Fig. 18(d) illustrates that, despite enforcing silent neighbors, a large portion of the wave energy still remains along the ground surface for the optimized loading time signals. In the ensuing experiments (cases 2B and 3B), we will discuss again the possibility of enforcing silent neighbors with large wave motions in the target by using independently-optimized wave sources in unsymmetric locations.

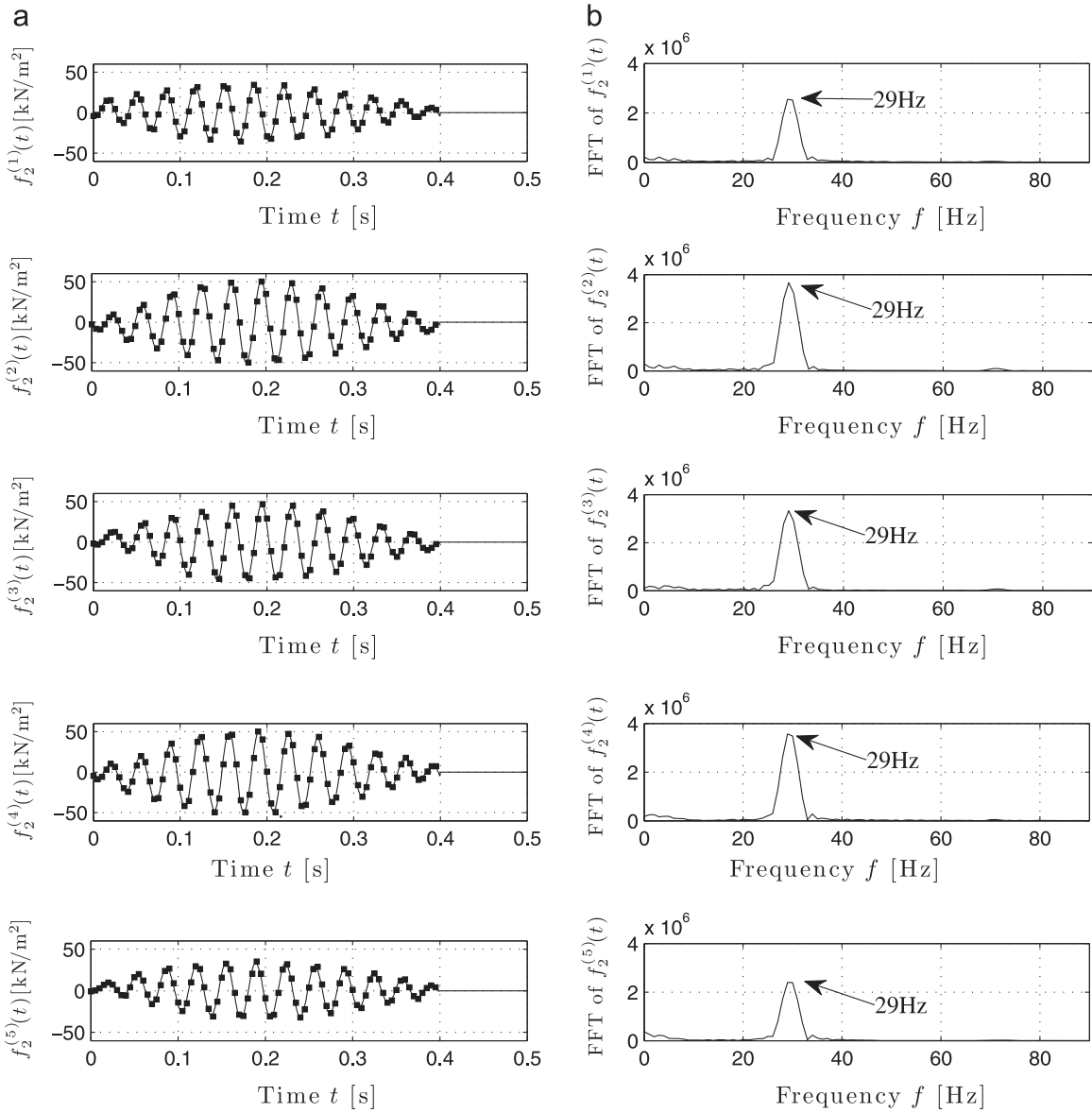


Fig. 14. The finally converged loading time signals of the five wave sources at unsymmetric locations for the formation model shown in Fig. 6(c) after 140 iterations of the optimization process for the maximization of the kinetic energy in Ω_0 with silent neighbors: (a) the finally converged signals and (b) the frequency spectra of the finally converged signals.

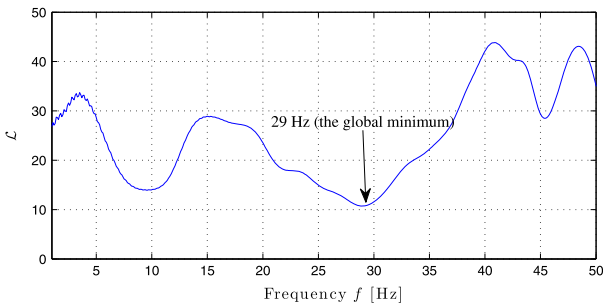


Fig. 15. Frequency sweep of the objective functional, (8), using a harmonic load $f_2(t) = 50 \sin(2\pi ft)$ kN/m² for the formation model shown in Fig. 6(c).

5.1.3. Two independent unsymmetric optimal wave sources for maximum kinetic energy in a target with silent neighbors (case 2B)

Next, we consider two strip surface loading wave sources situated in unsymmetric locations – the centroids of the strip loading areas are located at (−30 m, 0 m) and (70 m, 0 m), respec-

tively – shown in Fig. 6(b). The total observation time is 2 s, and the time step is 0.001 s; we temporally discretize an initial perturbation-like loading time signal $f_2(t)$ for each wave source by using 40 quadratic elements (80 discretized force parameters). It is also considered that, in this case (2B), only the first 0.3 s of the force signal will be updated (i.e., $f(t) = 0$ for $t > 0.3$ s). By inverting loading time signals of such a short duration (0.3 s vs 2 s in the cases 1A and 1B), we wish to investigate whether inverting for time signals of a short duration can successfully recover the amplification frequencies.

We start with two identical initial guesses for the loading time signals (Fig. 11(a)) at the two loading locations. The loading time signal for each wave source changes independently during the iteration procedure, i.e., $f_2^{(1)}(t) \neq f_2^{(2)}(t)$ (see Fig. 11 (c)). Here, $f_2^{(1)}(t)$ and $f_2^{(2)}(t)$ denote independent loading signals of the strip loading wave sources, whose centroids are located at $x_1 = -30$ and 70 m, respectively. Since each time signal is discretized by 80 force parameters, we are inverting for optimal values of 160 force parameters. By inverting two wave source signals of unsymmetric

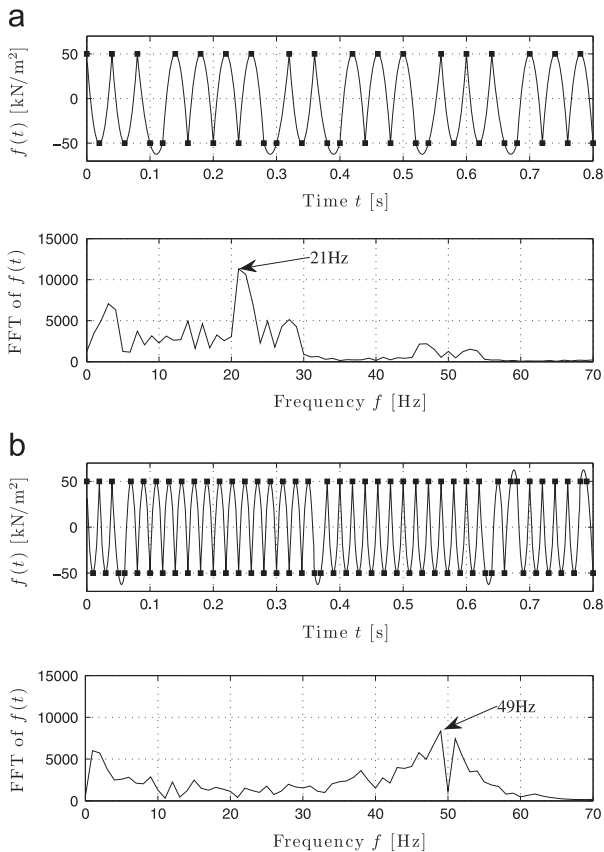


Fig. 16. The finally converged optimal loading signals that maximize the acceleration fields within a target: (a) the loading signal discretized by using 100 force parameters and (b) the loading signal discretized by using 200 force parameters.

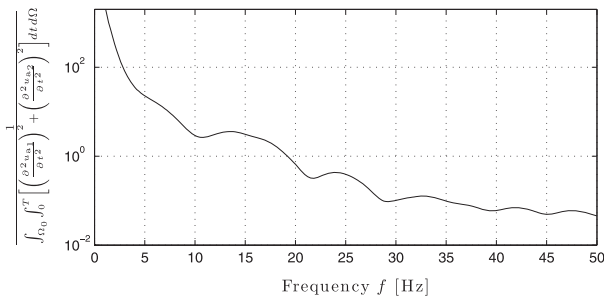


Fig. 17. Frequency sweep of the objective functional, (9), using a harmonic load $f_2(t) = 50 \sin(2\pi ft)$ kN/m² for the formation model shown in Fig. 6(a).

locations independently, we wish to examine whether the spectra of the independent wave source signals differ.

After the first 36 iterations, the optimizer arrives at the time signals, whose dominant frequencies are 10.3 Hz and 28.3 Hz for both $f_2^{(1)}(t)$ and $f_2^{(2)}(t)$ (Fig. 11(c, d)). However, after the 80th iteration, the time signals converge into pulses, whose dominant frequencies are 8.8 Hz (Fig. 11(e, f)). That is, the optimizer first converges to a local minimum basin associated with dominant frequencies 10.3 and 28.3 Hz, and then converges to another local minimum basin with a dominant frequency of 8.8 Hz after about 80 iterations (see the distribution of the objective functional (8), with respect to the frequency f of the $f_2^{(1)}(t) = f_2^{(2)}(t) = 50 \sin(2\pi ft)$ kN/m² in Fig. 12). Fig. 11(e) shows that the converged signals are nearly identical to each other. In this experiment too, despite the unsymmetric placement of the sources and the

independent way they operate (their source characteristics were independently updated), the optimized signals are still dominated by the formation's amplification frequencies.

Fig. 18(e) shows that, even though the final converged loading time signals lead to small surface wave energy, the kinetic energy within the target inclusion is also much smaller than that corresponding to the previously optimized loading signals shown in cases 1A and 1B, essentially due to the enforcement of silent neighbors.

5.1.4. Five independent unsymmetric optimal wave sources for maximum kinetic energy in a target with silent neighbors (case 3B)

Next, we consider five independent wave sources located at unsymmetric locations, as shown in Fig. 6(c). Here, $f_2^{(1)}(t)$, $f_2^{(2)}(t)$, $f_2^{(3)}(t)$, $f_2^{(4)}(t)$, and $f_2^{(5)}(t)$ denote independent loading time signals of the strip loading wave sources whose centroids are located at $x_1 = -96, -38, 0, 48,$ and 81 m, respectively, on the ground surface ($x_2 = 0$ m).

The total observation time is 2 s, and the time step is 0.001 s; we discretize the loading signal of each source by using 40 quadratic elements (80 discretized force parameters) for a duration of 0.4 s. The optimization process starts with five different initial guesses with perturbation-like time signals, as shown in Fig. 13(a); the frequency spectra of the initial signals are shown in Fig. 13(b). After 140 iterations, the optimizer arrives at the loading signals shown in Fig. 14(a) with the frequency spectra shown in Fig. 14(b). We remark that the finally converged loading signals are all nearly sinusoidal with a strong dominant frequency of 29 Hz (the frequency accountable for the global minimum of the objective functional (8), as shown in Fig. 15), while their phase angles, corresponding to the dominant frequency 29 Hz, differ for each converged loading signal.

Fig. 18(f) shows that using five unsymmetric wave sources with the optimized loading signals leads to a clear illumination of the target inclusion, with an even more effective minimization of the surface wave energy than in previous experiments (Fig. 18(f) versus (d, e)). Clearly, wave sources, operating at optimal locations and timings, would lead to a better wave-energy focusing within a target formation than non-optimally placed wave sources.

Similar to the experiment 2B, this optimization process, using independently-optimized loading signals for five wave sources unsymmetrically placed, also resulted in signals whose spectra feature a clear dominant frequency for all five wave sources. Though we expect the formation's amplification frequencies to have a dominant role in the source signals, we also expect that constructive interference patterns at a target inclusion will alter the temporal and (somewhat less) the frequency content of the optimal signals. Thus, we expect that source placement is of importance, even though it is not revealed in these experiments due to the symmetric nature of the synthetic example formation.

5.1.5. Two symmetric optimal wave sources for maximum acceleration field within a target (case 1C)

Next, we seek to maximize the acceleration field within a target inclusion Ω_0 , by minimizing the acceleration-based objective functional (9), for the formation model subjected the two symmetric ground wave sources, as shown in Fig. 6(a). The total observation time is 2 s, and the time step is 0.001 s. The two symmetric wave sources are optimized synchronously. Two numerical experiments are carried out: first, we inverted the force signal discretized by 100 force parameters; second, we inverted the force signal discretized by 200 force parameters.

Fig. 16(a, b) shows that the two optimization experiments, using 100 and 200 discretized force parameters, yield loading signals with dominant frequencies 21 and 49 Hz, respectively. It should be noted that a higher dominant frequency is recovered when a higher number

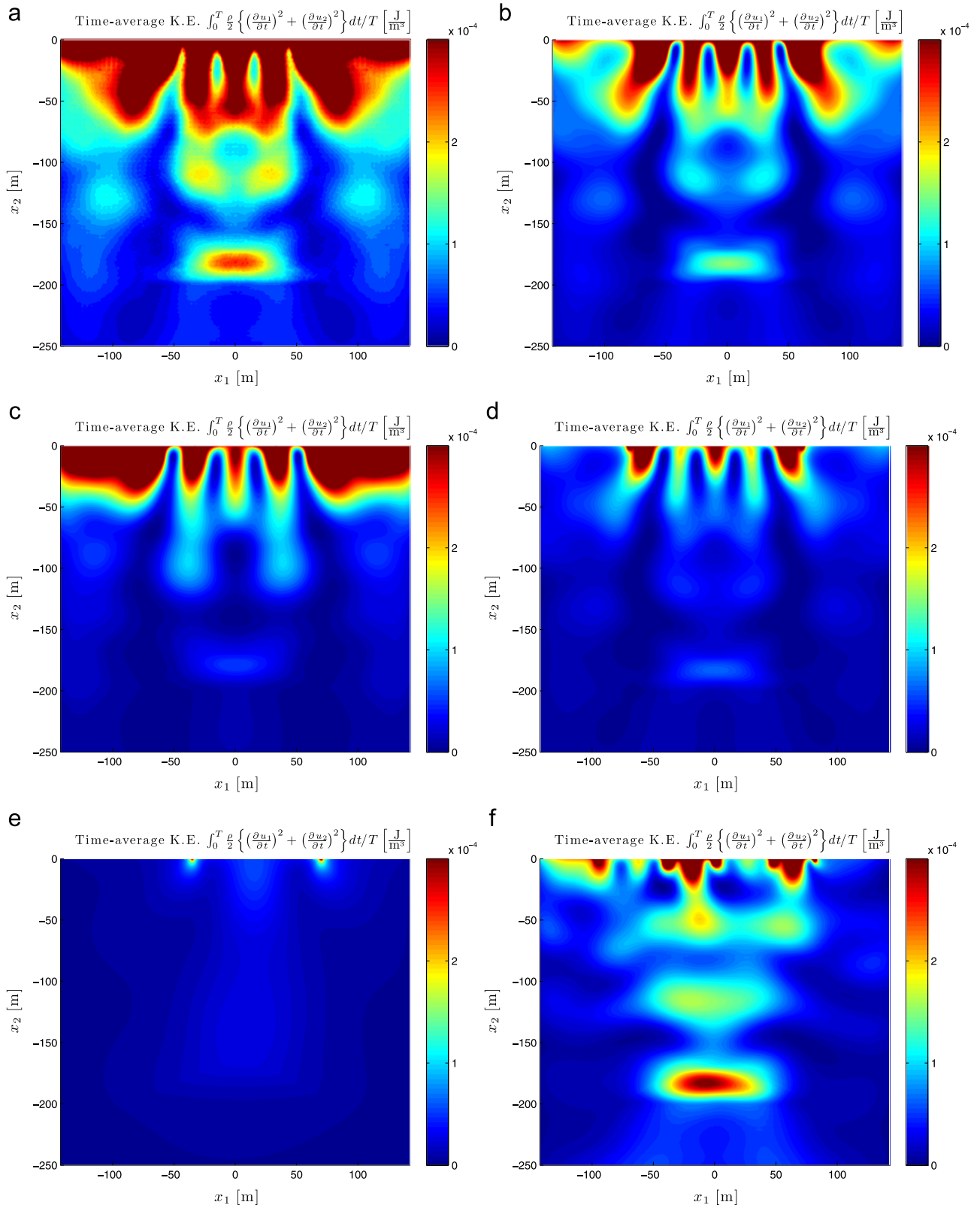


Fig. 18. The spatial distributions of $\int_0^T \rho/2 \{ (\partial u_1 / \partial t)^2 + (\partial u_2 / \partial t)^2 \} dt / T$ (J/m³, the time-averaged kinetic energy, in Ω_{reg} induced by, respectively, (a) the optimized loading in case 1A, (b) the sinusoidal loading $f_2(t) = 50 \sin(2\pi \times 29t)$ kN/m² that employs the dominant frequency of the optimized signal in case 1A, (c) a non-optimal sinusoidal loading $f_2(t) = 50 \sin(2\pi \times 25t)$ kN/m², using a non-optimal frequency $f = 25$ Hz, of two symmetric wave sources (Fig. 6(a)), (d) the optimized loading in case 1B, (e) the optimized loadings in case 2B, and (f) the optimized loadings in case 3B.

of discrete force parameters is used. We remark that the amplitude of the acceleration field within the target inclusion Ω_0 tends to be greater for a higher frequency (the frequency sweep of (9), shown in Fig. 17, demonstrates that the value of the acceleration-based objective functional (9) tends to be smaller for a higher frequency). Thus, the optimizer, for the acceleration-based objective functional (9), leads to an optimal loading time signal showing a dominant frequency, which is nearly identical to the highest dominant frequency the temporal discretization can support. Overall, if one is interested in maximizing the acceleration field, the higher the frequency the stronger the acceleration is.

5.2. Feasibility of dislodging trapped oil droplets

To investigate the feasibility of dislodging trapped oil droplets within the target inclusion in the formation model shown in Fig. 6, we used the values of threshold acceleration levels for different frequencies, shown in Table 2, evaluated by using the latest threshold model (Beresnev and Deng, 2010; Deng and Cardenas, 2013).

Table 2

Threshold acceleration levels evaluated by using Beresnev's latest threshold acceleration model (Beresnev and Deng, 2010; Deng and Cardenas, 2013), as well as the fluid-saturated porous permeable rock properties shown in Table 3.

Frequency (Hz)	Threshold acceleration (m/s ²)
10	0.4
20	0.7
30	1
40	1.3
50	1.6

Table 3

Fluid-saturated porous permeable rock properties utilized for evaluating the threshold acceleration values for the mobilization of trapped oil droplets.

Maximum pore radius r_{\max}	200 micron
Minimum pore radius r_{\min}	100 micron
Background pressure gradient	35,185 Pa/m
Water viscosity	1 cp
Oil viscosity	5 cp
Capillary pressure	800 Pa
Interface tension σ	40 dyne/cm=0.04 N/m

Table 4

Summary of our numerical experiments.

Case number	Wave source locations	Maximized metric in the reservoir Ω_0	Dominant frequency of optimized loading (Hz)	Time-averaged kinetic energy in Ω_0 (J/m ³)	Maximum amplitude $\frac{\partial^2 u}{\partial t^2}$ in Ω_0 (m/s ²)
1A	Symmetric two sources located at $x_1 = -70, 70$ m (Fig. 6(a))	Kinetic energy (all layers active)	29	3×10^{-4}	1.0
1B		Kinetic energy (silent neighbors)	29.5	8×10^{-5}	0.1
1C		Acceleration (all layers active)	49	1×10^{-4}	0.6
2A	Unsymmetric two sources located at $x_1 = -30, 70$ m (Fig. 6(b))	Kinetic energy (all layers active)	28.5	1×10^{-4}	0.5
2B		Kinetic energy (silent neighbors)	8.8	2×10^{-5}	0.02
2C		Acceleration (all layers active)	50	1×10^{-4}	0.6
3A	Unsymmetric five sources located at $x_1 = -96, -38, 0, 48, 81$ m (Fig. 6(c))	Kinetic energy (all layers active)	29	1.4×10^{-3}	1.2
3B		Kinetic energy (silent neighbors)	29	3×10^{-4}	0.2
3C		Acceleration (all layers active)	45	3×10^{-4}	1.2

2013) (the model is taking into account the viscosity of pore fluid), as well as realistic values for the fluid-saturated porous permeable rock properties shown in Table 3.

In Table 3: (a) r_{\max} and r_{\min} denote the maximum and minimum radii, respectively, of the cross-section of pore space in an axisymmetric sinusoidally constricted pore channel; (b) the background pressure gradient 35,185 Pa/m corresponds to a Darcy flow-rate of 1 ft/day of fluid of viscosity 1cp within a porous permeable rock of permeability 100 md; and (c) the capillary pressure, i.e., $P_c = 2\sigma \cos \theta/r$, of 800 Pa corresponds to interface tension σ of 0.04 N/m, a radius of curvature r of 100 micron, and an oil/water contact angle θ of 0°.

The threshold values shown in Table 2 are up to 1.6 m/s², for frequencies up to 50 Hz. A summary of the optimization results in Table 4 shows that the optimized loadings in the optimization cases 1A, 3A, and 3C produced acceleration field whose amplitude is as large as the threshold values. Thus, these optimized loads could initiate the dislodging-based mobilization of the trapped oil droplets within a fluid-saturated porous permeable rock in the target shallow reservoir model of Fig. 6. We also suggest that the mobilization of trapped oil droplets for this subsurface formation model (or potentially even for deeper reservoir formation models) could be further facilitated if (i) sources are optimally placed, in addition to be operated at the optimized signals, (ii) a combination of surficial and downhole wave sources are employed, especially for deeper reservoirs, and (iii) vibrational stimulation is combined with another EOR method, e.g., low-concentration surfactant injection, which could lower the fluid viscosity of target reservoir formations (Jeong et al., 2014).

6. Discussion

This section discusses the key findings from the numerical results. Our observations from the numerical experiments address the questions posed in the Introduction, as follows.

6.1. Characteristic amplification frequencies

Table 4 shows that there is a dominant amplification frequency of 29 Hz that leads to the maximization of the kinetic energy within the reservoir Ω_0 in almost all the cases, and under a variety of loading conditions. The particular frequency, as shown by the

frequency sweep, corresponds to one of the discrete amplification frequencies of the formation. It is not a resonant frequency in the classical sense (i.e., a frequency for which the motion becomes unbounded under undamped conditions), since the medium is semi-infinite in extent, but, rather, a frequency that will generate a large response. The frequency depends on the formation's characteristics (geometry, properties, etc.). This amplification frequency can be obtained either by the optimization procedure described herein, or by conducting a frequency sweep (i.e., an objective functional versus frequency).

It is also observed that the temporal discretization of the initially-guessed loading time signal controls the frequency content of the optimal loading signal that can maximize the acceleration within the reservoir. In short, a greater number of force parameters is likely to lead to optimized loading signals of a higher dominant frequency for maximizing the acceleration field within a target reservoir.

6.2. Dependency of source-inversion on the locations of surface wave sources

It appears that the locations of the wave sources are critical in arriving at motion maximization, in particular, in the case of relatively silent neighbors. For example, as was seen in the cases of two wave sources, there is a significant shift of the dominant frequency of the optimized signals from 29 Hz (two symmetric sources, case 1B), to 8.8 Hz (two unsymmetric sources, case 2B). Moreover, optimizing the five unsymmetric wave sources, in case 3B, leads to more significant reduction of the energy concentration near the surface, as well as better focusing and illumination of the target reservoir than the other cases. Thus, we conjecture that optimally located sources could produce a stronger wave-energy focusing effect than non-optimally located sources operating at the reservoir's amplification frequency. Though not explored in this work, it is possible to enhance the presented optimization process to include a search for the optimal placement of the wave sources as well.

6.3. Frequency spectra of independently-optimized multiple wave sources

Even with multiple independent wave sources at unsymmetric locations, our optimizer produced optimal excitation signals with a single dominant frequency – the dominant reservoir's amplification frequency. Thus, we conjecture that multiple monochromatic sources operating at one of the reservoir's amplification frequencies, even if not optimally placed, will still result in significant motion within the target reservoir. Though not shown here, we expect that the optimizer will produce signals with different spectra when faced with a highly heterogeneous formation.

6.4. Feasibility of the wave-induced oil mobilization within a target formation

We have used the results of a previously published threshold acceleration model on oil mobility to evaluate whether the motion resulting from the solution of the inverse source problem could indeed result in oil mobilization. For most of our simulations, we used the kinetic energy as the metric to be maximized, but also produced results where we sought to maximize the acceleration field at the target formation. Under certain conditions (shallow reservoirs), the induced motion meets the acceleration threshold.

7. Conclusions

We explored, via computational modeling, the possibility of inducing a resonance-like wave motion within a target reservoir formation to increase oil mobility, and therefore, allow for recovery, where none could previously be possible. To this end, we presented a systematic framework, based on casting the associated mathematical problem as an inverse source optimization problem. In particular, we demonstrated via numerical experiments that the developed algorithm can robustly find optimal wave source signals that maximize the kinetic energy, acceleration, or another desired mobility metric, at the target formation. The results of a previously published threshold acceleration model on oil mobility are used to evaluate whether the motion resulting from the solution of the inverse source problem could indeed result in oil mobilization.

The numerical results present the following key findings. First, optimal signals, of which frequency spectra include characteristic amplification frequencies, could maximize the kinetic energy or acceleration field (or any desired metrics) in a target reservoir. The amplification frequency depends on the formation's characteristics (geometry, properties, etc.). The optimal source signals of multiple wave sources are very likely to have a very similar spectrum for each source. Second, locations of surface wave sources are critical for the optimal loading signals and their frequency spectra distribution, as well as the extent to which desired effects (e.g., wave energy focusing with silent neighbors) in a target reservoir are maximized. Third, wave energy could be focused within the target reservoir area, while simultaneously minimizing the disturbance to neighboring formations. Lastly, the wave motion, induced by the optimized surface wave sources, is large enough to result in the mobilization of trapped oil droplets within a shallow target formation.

Acknowledgments

This work was partially supported by an Academic Excellence Alliance grant between the King Abdullah University of Science and Technology (KAUST) and the University of Texas at Austin, by the Society of Petroleum Engineers STAR Fellowship, and the William S. Livingston Fellowship at the University of Texas at Austin awarded to the first author. This support is gratefully acknowledged.

References

- Amro, M.M., Al-Mobarky, M.A., Al-Homadi, E.S., 2007. Improved oil recovery by application of ultrasound waves to waterflooding. In: SPE Middle East Oil and Gas Show and Conference, SPE 105370-MS, Society of Petroleum Engineers, Kingdom of Bahrain.
- Averbakh, V.S., Vlasov, S.N., Zaslavsky, Y.M., 2000. Motion of a liquid droplet in a capillary under the action of static force and an acoustic field. *Radiophys. Quantum Electron.* 43, 142–147.
- Bachrach, R., Nur, A., Agnon, A., 2001. Liquefaction and dynamic poroelasticity in soft sediments. *J. Geophys. Res.* 106, 13515–13526.
- Barabanov, V.I., Pavlov, M.V., 2009. Increasing oil production from depleted fields through seismic stimulation. *First Break* 27, 97–102.
- Beckham, R.E., Abdel-Fattah, A., Roberts, P.M., Ibrahim, R., Tarimala, S., 2010. Mobilization of colloidal particles by low-frequency dynamic stress stimulation. *Langmuir* 26, 19–27.
- Beresnev, I., Gaul, W., Vigil, R.D., 2011. Direct pore-level observation of permeability increase in two-phase flow by shaking. *Geophys. Res. Lett.* 38.
- Beresnev, I.A., 2006. Theory of vibratory mobilization on nonwetting fluids entrapped in pore constrictions. *Geophysics* 71, 47–56.
- Beresnev, I.A., Deng, W., 2010. Viscosity effects in vibratory mobilization of residual oil. *Geophysics* 75, 79–85.
- Beresnev, I.A., Johnson, P., 1994. Elastic-wave stimulation of oil production: a review of methods and results. *Geophysics* 59, 1000–1017.
- Biot, M.A., 1956. Theory of propagation of elastic waves in a fluid-saturated porous solid. I. Low-frequency range. *J. Acoust. Soc. Am.* 28, 168–178.

- Bremmer, C., Harris, G., Kosmala, A., Nicholson, B., Ollre, A., Pearcy, M., Salmas, C.J., Solanki, S.C., 2006. Evolving technologies: electrical submersible pumps. *Schlumberger Oilfield Rev.*, 30–43.
- Deng, W., Cardenas, M.B., 2013. Dynamics and dislodgment from pore constrictions of a trapped nonwetting droplet stimulated by seismic waves. *Water Resour. Res.* 49, 4206–4218.
- Elkhoury, J.E., Brodsky, E.E., Agnew, D.C., 2006. Seismic waves increase permeability. *Nature* 441, 1135–1138.
- Elkhoury, J.E., Niemeijer, A., Brodsky, E.E., Marone, C., 2011. Laboratory observations of permeability enhancement by fluid pressure oscillation of in situ fractured rock. *J. Geophys. Res.: Solid Earth* (1978–2012) 116.
- Fathi, A., Poursartip, B., Kallivokas, L.F., 2015. Time-domain hybrid formulations for wave simulations in three-dimensional PML-truncated heterogeneous media. *Int. J. Numer. Methods Eng.* 101, 165–198.
- Fletcher, R., Reeves, C.M., 1951. Function minimization by conjugate gradients. *Comput. J.* 7, 149–154.
- Gassmann, F., 1951. Über die elastizität poroser medien. *Veierteljahrsschrift der Naturforschenden Gesellschaft in Zurich* 96, 1–23.
- Geballe, Z., Wang, C.Y., Manga, M., 2011. A permeability-change model for water-level changes triggered by teleseismic waves. *Geofluids* 11, 302–308.
- Groenenboom, J., Wong, S., Meling, T., Zschuppe, R., Davidson, B., 2003. Pulsed water injection during waterflooding. In: *International Improved Oil Recovery Conference in Asia Pacific*, SPE 84856, Society of Petroleum Engineers, Kuala Lumpur, Malaysia.
- Guo, X., Du, Z., Li, G., Shu, Z., 2004. High frequency vibration recovery enhancement technology in the heavy oil fields of China. In: *SPE International Thermal Operations and Heavy Oil Symposium and Western Regional Meeting*, SPE 86956, Society of Petroleum Engineers, Bakersfield, California.
- Hamida, T., Babadagli, T., 2005a. Capillary interaction of different oleic and aqueous phases between matrix and fracture under ultrasonic waves. In: *SPE Europe/EAGE Annual Conference*, SPE 94105, Society of Petroleum Engineers, Madrid, Spain.
- Hamida, T., Babadagli, T., 2005b. Effect of ultrasonic waves on the capillary imbibition recovery of oil. In: *SPE Asia Pacific Oil and Gas Conference and Exhibition*, SPE 92124, Society of Petroleum Engineers, Jakarta, Indonesia.
- Hamida, T., Babadagli, T., 2005c. Effects of ultrasonic waves on immiscible and miscible displacement in porous media. In: *SPE Annual Technical Conference and Exhibition*, SPE 95327, Society of Petroleum Engineers, Dallas, Texas.
- Hilpert, M., Jirka, G.H., Plate, E.J., 2000. Capillarity-induced resonance of oil blobs in capillary tubes and porous media. *Geophysics* 65, 874–883.
- Huh, C., 2006. Improved oil recovery by seismic vibration: a preliminary assessment of possible mechanisms. In: *International Petroleum Conference*, SPE 103870, Society of Petroleum Engineers, Cancun, Mexico.
- Iassonov, P.P., Beresnev, I.A., 2003. A model for enhanced fluid percolation in porous media by application of low-frequency elastic waves. *J. Geophys. Res.* 108, 2138–2146.
- Jeong, C., Huh, C., Kallivokas, L.F., 2011. On the feasibility of inducing oil mobilization in existing reservoirs via wellbore harmonic fluid action. *J. Pet. Sci. Eng.* 76, 116–123.
- Jeong, C., Huh, C., Kallivokas, L.F., Lake, L.W., et al., 2014. Estimation of oil production rates in reservoirs exposed to focused vibrational energy. *SPE Improved Oil Recovery Symposium*.
- Jeong, C., Kallivokas, L.F., Huh, C., Lake, L.W., 2010. Optimization of sources for focusing wave energy in targeted formations. *J. Geophys. Eng.* 7, 242–256.
- Kalinski, M.E., 2007. Effect of vibroseis arrays on ground vibrations: a numerical study. *J. Environ. Eng. Geophys.* 12, 281–287.
- Kallivokas, L.F., Fathi, A., Kucukcoban, S., Stokoe II, K.H., Bielak, J., Ghattas, O., 2013. Site characterization using full waveform inversion. *Soil Dyn. Earthq. Eng.* 47, 62–82.
- Kang, J.W., Kallivokas, L.F., 2010. Mixed unsplit-field perfectly matched layers for transient simulations of scalar waves in heterogeneous domains. *Comput. Geosci.* 14, 623–648.
- Kostrov, S., Wooden, W., 2005. In situ seismic stimulation shows promise for revitalizing mature fields. *Oil Gas J.*, 2–25.
- Kostrov, S., Wooden, W., 2008. Possible mechanisms and case studies for enhancement of oil recovery and production using in-situ seismic stimulation. In: *SPE/DOE Symposium on Improved Oil Recovery*, SPE 114025, Society of Petroleum Engineers, Tulsa, Oklahoma, USA.
- Kouznetsov, O.L., Simkin, E.M., Chilingar, G.V., Katz, S.A., 1998. Improved oil recovery by application of vibro-energy to waterflooded sandstones. *J. Pet. Sci. Eng.* 19, 191–200.
- Kucukcoban, S., 2010. The Inverse Medium Problem in PML-Truncated Elastic Media (Doctoral dissertation). The University of Texas at Austin.
- Kucukcoban, S., Kallivokas, L.F., 2011. Mixed perfectly-matched-layers for direct transient analysis in 2D elastic heterogeneous media. *Comput. Methods Appl. Mech. Eng.* 200, 57–76.
- Kucukcoban, S., Kallivokas, L.F., 2013. A symmetric hybrid formulation for transient wave simulations in PML-truncated heterogeneous media. *Wave Motion* 50, 57–79.
- Kuznetsov, O.L., Simkin, E.M., Chilingar, G.V., Gorfunkel, M.V., Robertson, J.O., 2002. Seismic techniques of enhanced oil recovery: experimental and field results. *Energy Source* 24, 877–889.
- Kuznetsov, V.V., Nikolaev, A.V., 1990. Elaboration of physical principles of vibroseismic action on oil reservoir (Razrabotka fizicheskikh osnov vibroseismicheskogo vozdeystviya na neftianouyou zalezhi). Report (in Russian). Institute of Physics of the Earth.
- Li, W., Vigil, R.D., Beresnev, I.A., Iassonov, P.P., Ewing, R., 2005. Vibration-induced mobilization of trapped oil ganglia in porous media: experimental validation of a capillary-physics mechanism. *J. Colloid Interface Sci.* 289, 193–199.
- Manga, M., Beresnev, I., Brodsky, E.E., Elkhoury, J.E., Elsworth, D., Ingebritsen, S., Mays, D.C., Wang, C.Y., 2012. Changes in permeability caused by transient stresses: field observations, experiments, and mechanisms. *Rev. Geophys.* 50.
- Nocedal, J., Wright, S., 2006. *Numerical Optimization*. Springer, New York, NY.
- Osika, D.G., 1981. Fluid Regime of Seismically Active Regions (Fluidniy Rejim Seismicheskii-aktivnikh Oblastey) (in Russian). Nauka Press, Moscow.
- Owens, W.W., Archer, D.L., 1966. Waterflood pressure pulsing for fractured reservoirs. *J. Pet. Technol.*, 745–752.
- Paulsson, B.N., 1989. Nondestructive Downhole Seismic Vibrator Source and Processes of Utilizing the Vibrator to Obtain Information about Geologic Formations (Patent number: 4805725). United States Patent.
- Roberts, P.M., Abdel-Fattah, A.I., 2009. Seismic stress stimulation mobilizes colloids trapped in a porous rock. *Earth Planet. Sci. Lett.* 284, 538–543.
- Roberts, P.M., Esipov, I.B., Majer, E.L., 2003. Elastic wave stimulation of oil reservoirs: promising EOR technology?. *Lead. Edge* 22, 448–453.
- Roberts, P.M., Sharma, A., Uddameri, V., Monagle, M., Dale, D.E., Steck, L.K., 2001. Enhanced DNAPL transport in a sand core during dynamic stress stimulation. *Environ. Eng. Sci.* 18, 67–79.
- Snimova, M.N., 1968. Effect of earthquakes on the oil yield of the Gudermes field (Northeastern Caucasus). *Izvestiya Academy of Sciences, USSR, Fizika Zemli (Physics of the Solid Earth)* 12, 71–76.
- Spanos, T., Shand, D., Davidson, B., Samaroo, M., Dusseault, M., 2003. Pressure pulsing at the reservoir scale: a new IOR approach. *J. Can. Pet. Technol.* 42, 16–28.
- Steinbrugge, K.V., Moran, D.F., 1954. An engineering study of the Southern California earthquake of July 21, 1952, and its aftershocks. *Bull. Seismol. Soc. Am.* 44, 279–283.
- Stirpe, M.T., Guzman, M.T., Manrique, E., Alvarado, V., 2004. Cyclic water injection simulations for evaluations of its potential in Lagocinco field. In: *SPE/DOE Symposium on Improved Oil Recovery*, Society of Petroleum Engineers, Tulsa, Oklahoma, USA.
- Surguchev, L., Koundin, A., Melberg, O., Rolfsvåg, T., Menard, W.P., 2002. Cyclic water injection: improved oil recovery at zero cost. *Pet. Geosci.* 8, 89–95.
- Thomas, J.M., Chrysikopoulos, C.V., 2007. Experimental investigation of acoustically enhanced colloid transport in water-saturated packed columns. *J. Colloid Interface Sci.* 308, 200–207.
- Vogler, E.T., Chrysikopoulos, C.V., 2004. An experimental study of acoustically enhanced NAPL dissolution in porous media. *Environ. Energy Eng.* 12, 3271–3280.
- Voytov, G.I., Osika, D.G., Grechukhina, T.G., Plotnikov, I.A., 1972. Some geological and geochemical consequences of the Daghestan earthquake of May 14, 1970. *Trans. USSR Acad. Sci. Earth Sci. Sect.* 202, 576–579.
- Westermark, R.V., Brett, J.F., Maloney, D.R., 2001a. Enhanced oil recovery with downhole vibration stimulation. In: *SPE Production and Operations Symposium*, SPE 67303-MS, Society of Petroleum Engineers, Oklahoma City, Oklahoma.
- Westermark, R.V., Brett, J.F., Maloney, D.R., 2001b. Using downhole vibration stimulation for enhanced oil recovery. *World Oil*, 57–66.
- Zhu, T., Xutao, H., 2005. Downhole harmonic vibration oil-displacement system: a new IOR tool. In: *SPE Western Regional Meeting*, SPE 94001-MS, Society of Petroleum Engineers, Irvine, California.